Oontawee *et al. BMC Veterinary Research* (2025) 21:31
https://doi.org/10.1186/s12917-024-04465-2

BMC Veterinary Research

RESEARCH

Open Access

Small extracellular vesicles derived from sequential stimulation of canine adipose-derived mesenchymal stem cells enhance anti-inflammatory activity

Saranyou Oontawee[1,2,3], Parkpoom Siriarchavatana[1,2,3], Watchareewan Rodprasert[2,3], Irma Padeta[2,3], Yudith Violetta Pamulang[2,3], Poorichaya Somparn[5], Trairak Pisitkun[5], Boondarika Nambooppha[6], Nattawooti Sthitmatee[6], Daneeya Na Nan[7,8], Thanaphum Osathanon[9,10,11], Hiroshi Egusa[12] and Chenphop Sawangmake[2,3,4,11*]

Abstract

Background Small extracellular vesicles (sEVs) derived from mesenchymal stem cells (MSCs) are recognized for their therapeutic potential in immune modulation and tissue repair, especially in veterinary medicine. This study introduces an innovative sequential stimulation (IVES) technique, involving low-oxygen gas mixture preconditioning using in vitro fertilization gas (IVFG) and direct current electrical stimulation (ES20), to enhance the anti-inflammatory properties of sEVs from canine adipose-derived MSCs (cAD-MSCs). Initial steps involved isolation and comprehensive characterization of cAD-MSCs, including morphology, gene expression, and differentiation potentials, alongside validation of the electrical stimulation protocol. IVFG, ES20, and IVES were applied simultaneously with a control condition. Stimulated cAD-MSCs were evaluated for morphological changes, cell viability, and gene expressions. Conditioned media were collected and purified for sEV isolation on Day1, Day2, and Day3. To validate the efficacy of IVES for sEV production, various analyses were conducted, including microscopic examination, surface marker assessment, zeta-potential measurement, protein quantification, nanoparticle tracking analysis, and determination of anti-inflammatory activity.

Results We found that IVES demonstrated non-cytotoxicity and induced crucial genotypic changes associated with sEV production in cAD-MSCs. Interestingly, IVFG influenced cellular adaptation, while ES20 induced hypoxia activation. By merging these stimulations, IVES enhanced sEV stability and quality profiles. The cAD-MSC-derived sEVs exhibited anti-inflammatory activity in lipopolysaccharide-induced RAW264.7 macrophages, emphasizing their improved effectiveness without cytotoxicity or immunogenicity. These effects were consistent across day 3 collection, indicating the establishment of an effective protocol for sEV production.

Conclusions This research established an innovative sequential stimulation method with positive impact on sEV characteristics including stability, quality, and anti-inflammatory activity. This study not only contributes to the enhancement of sEV production but also sheds light on their functional aspects for therapeutic interventions.

*Correspondence:
Chenphop Sawangmake
chenphop.s@chula.ac.th
Full list of author information is available at the end of the article

Keywords Small extracellular vesicles, Canine, Mesenchymal stem cells, Sequential stimulation, Anti-inflammatory activity

Background

In the past decade, inflammatory diseases in dogs, including conditions like inflammatory bowel disease, type 1 diabetes mellitus, atopic dermatitis, and arthritis, have surged [1–4]. Small extracellular vesicles (sEVs) derived from canine adipose tissue mesenchymal stem cells (cAD-MSCs), sized between 50 and 300 nm, offer a promising intervention with robust anti-inflammatory properties [5–7]. Systemic and topical administrations of cAD-MSC-derived sEVs present an avenue to modulate inflammation for enhanced therapeutic outcomes [3, 8], prompting a growing interest in biophysical stimulation for cellular modulation [9–11]. The absence of exogenous substances in the biophysical stimulation protocols minimizes the risk of unintended contamination, allowing for precise modulation of cellular activities [12].

In MSC-based therapies, maintaining cell viability and functionality during stimulation protocols is crucial for ensuring the safety and efficacy of therapeutic products. Non-cytotoxic stimulation techniques offer a compelling alternative, allowing for precise control over cellular responses while preserving cell integrity [13]. Among these stimulations, hypoxic treatment significantly influences anti-inflammatory properties by macrophage polarization [6, 14], while pre-conditioning with low-oxygen gas mixture, in vitro fertilization gas, induces cellular alterations through hypoxia activation or adaptation mechanisms [15–19]. Direct current electrical stimulation, impacting MSC proliferation, migration, and differentiation, modulates cells through plasma membrane ion channels or ATP/Ca^{2+} oscillations [12, 13, 20–24]. The electrochemical reactions also have a possibility to modify cell culture environment by producing faradaic by-products [25]. Notably, the combined application of cyclic strain and electrical stimulation has shown significant efficacy in enhancing the neural differentiation of MSCs [10]. Hence, the development of innovative stimulation protocols for sEV production holds critical importance in driving forward the field of regenerative medicine.

This study pioneers a novel approach by introducing sequential stimulation, which combines low-oxygen gas mixture preconditioning with direct current electrical stimulation. The objective is to augment the anti-inflammatory properties of cAD-MSC-derived sEVs. By delving into the intricate relationship between biophysical stimulation and anti-inflammatory effects, this research not only aims to optimize sEV production but also to advance the landscape of canine therapy.

Results

Isolation and characterization of canine adipose-derived mesenchymal stem cells (cAD-MSCs)

In this study, cAD-MSCs were isolated from adipose tissues collected from healthy donors following approved protocols. Phase-contrast microscopy revealed adherent cells with fibroblastic morphology (Fig. 1A). Flow cytometry confirmed MSC-related surface markers (CD29: 99.69 ± 0.08%, CD44: 99.67 ± 0.02%, CD90: 94.94 ± 0.19%) and absence of the hematopoietic marker CD45 (1.54 ± 0.03%) (Fig. 1B). RT-qPCR analysis demonstrated the expression of stemness-related mRNA markers, *Oct4* ($4.62 \times 10^{-5} \pm 1.65 \times 10^{-5}$ AU) and *Rex1* ($15.37 \times 10^{-4} \pm 1.92 \times 10^{-4}$ AU), along with the proliferative marker *Ki-67* ($14.85 \times 10^{-4} \pm 6.16 \times 10^{-4}$ AU) (Fig. 1C).

Subculture analysis from passage 3 to 5 showed a consistent increase in population doubling time (PDT), with a rate of 3.50 days/passage and an adjusted R^2 of 1.00 (Fig. 1D). PDT reached 11.44 days at passage 5, indicating practical expansion capacity. Multi-lineage differentiation assays confirmed adipogenic, osteogenic, and chondrogenic potential. Adipogenesis resulted in lipid droplet accumulation and upregulation of *Lep* (2.03 ± 0.33 AU) and *Lpl* (2.64 ± 0.54 AU) (p-value ≤ 0.05) (Fig. 1E). Osteogenesis showed extracellular mineralization and upregulated *Runx2* (4.23 ± 0.05 AU), but *Ocn* (0.33 ± 0.06 AU) was not significantly upregulated (Fig. 1F). Chondrogenesis revealed glycosaminoglycan accumulation with trends in *Col2a1* expression (1.02 ± 0.09 AU), but minimal *Sox9* expression (0.05 ± 0.01 AU) (Fig. 1G).

These findings confirmed the MSC properties of the isolated cAD-MSCs, including morphology, marker expression, and differentiation potential. Cells in passages 3–5 were selected for subsequent experiments based on optimal subculture capacity.

Establishment of electrical stimulation protocol for small extracellular vesicle (sEV) production by cAD-MSCs

Screening for a non-cytotoxic voltage was conducted to establish a direct current (DC) electrical stimulation protocol for sEV production by cAD-MSCs. A schematic overview of the experiment is shown in Fig. 2A, with the experimental setup depicted in Fig. 2B. Cells were expanded in DMEM with 10% FBS for 6 days before

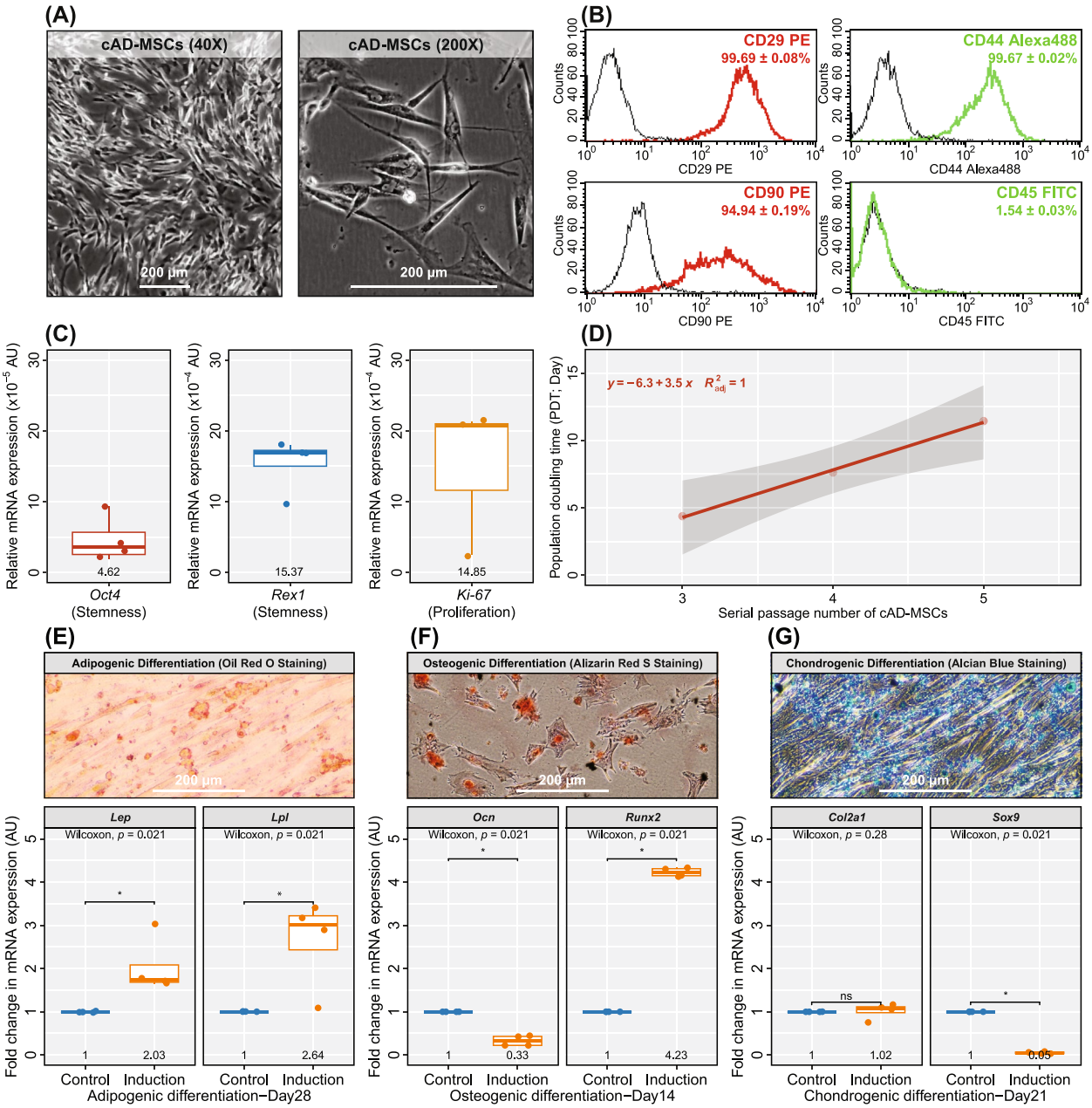

Fig. 1 Characterization of canine adipose-derived mesenchymal stem cells (cAD-MSCs) used in this study. **A** Morphology of cAD-MSCs were observed under a phase-contrast microscope at 40X and 100X magnifications. **B** Flow cytometer was used for characterization the presence of MSC markers (CD29, CD44, and CD90), and the leukocyte common antigen (CD45) on the cell surface. **C** Expression of the stemness-related genes (*Oct4* and *Rex1*) and the proliferation gene (*Ki-67*) were revealed by RT-qPCR with *Gapdh* normalization. **D** Population doubling time of cAD-MSCs in different serial passage numbers was estimated by counting cAD-MSCs after trypsinization. The linear regression curve was visualized along with a grey region of 95% confidence interval. The equation indicates the senescence rate as a slope with an annotation of the adjusted coefficient of determination (R_{adj}^2). **E** Adipogenic differentiation potential at day 28 post-induction was affirmed by Oil Red O staining and adipogenic related-mRNA expression (*Lep* and *Lpl*). **F** Osteogenic differentiation potential after 14-day induction was revealed by Alizarin Red S staining and the expression of osteogenic mRNA markers (*Ocn* and *Runx2*). **G** Chondrogenic differentiation potential at day 21 post-induction was assessed by Alcian Blue staining and chondrogenic mRNA markers (*Col2a1* and *Sox9*). The mRNA expressions for multi-lineage differentiation were normalized with the reference gene (*Gapdh*) and the undifferentiation control. The scale bars represent 200 µm. In boxplots, mean values of each group were annotated at the bottom, and global statistics were stated at the top. The bars indicate pairwise comparisons (ns; no significance or *p*-value > 0.05, *; *p*-value ≤ 0.05). Abbreviation: AU; arbitrary unit

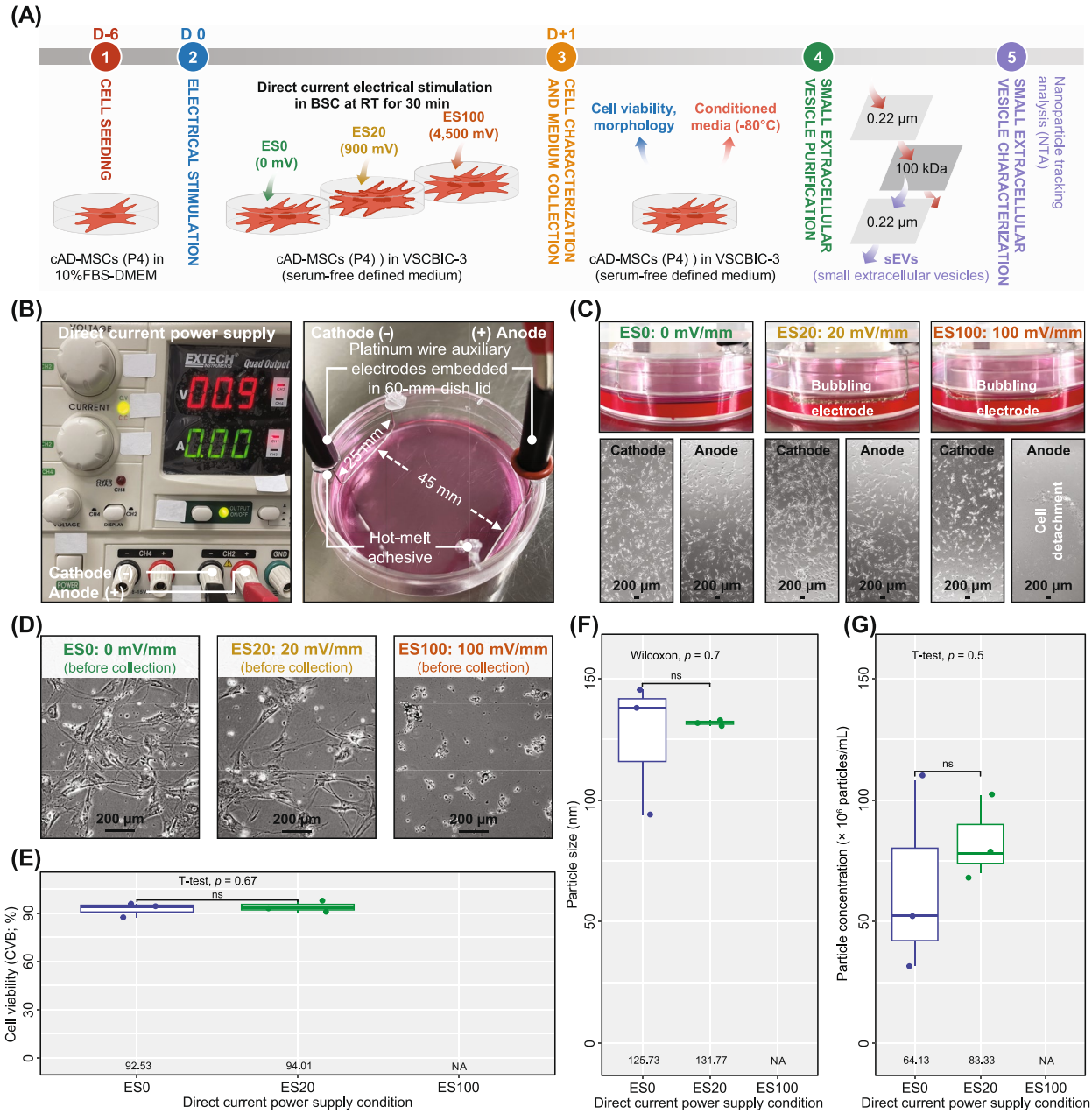

Fig. 2 Establishment of electrical stimulation protocol for small extracellular vesicle (sEV) production by cAD-MSCs. **A** The schematic diagram of the protocol for electrical stimulation of cAD-MSCs, as well as the following collection and purification of sEVs. **B** The experimental setup was accomplished by using platinum wire auxiliary electrodes embedded in a 60-mm dish lid as an anode and cathode, spaced 45 mm apart. The direct current power supply was used to apply experimental voltages to the cells via the electrodes and culture media. **C** The characteristics of the electrodes during stimulation were observed, and the morphological appearances of cAD-MSCs after treatments and (**D**) before conditioned medium collection were revealed with a phase-contrast microscope. The scale bars represent 200 µm. **E** The cell viability after stimulation was assessed by trypan blue exclusion assay. Nanoparticle tracking analysis was used to characterize (**F**) particle size and (**G**) particle concentration of sEV samples obtained from different voltage supplies. In boxplots, mean values of each group were annotated at the bottom, and global statistics were stated at the top. The bars indicate pairwise comparisons (ns; no significance or *p*-value > 0.05). Abbreviation: ES0; electrical stimulation at 0 mV/mm, ES20; electrical stimulation at 20 mV/mm, and ES100; electrical stimulation at 100 mV/mm, and NA; the data is not available

switching to serum-free defined medium (VSCBIC-3) for stimulation. During electrical stimulation using a 45-mm spaced electrode lid, electrolysis bubbles were observed around the platinum electrodes at 20 (ES20) and 100 (ES100) mV/mm power supplies, confirming the presence of an electrical field (Fig. 2C-top) [26].

Following a 30-min stimulation, cells in the anode area of ES100 detached and showed morphological changes, suggesting cell lysis (Fig. 2C-bottom). After 24 h, ES20-treated cells retained fibroblastic morphology similar to untreated controls (ES0), whereas ES100-treated cells did not (Fig. 2D). Based on these findings, ES100 (4,500 mV) was excluded from further analysis due to its cytotoxicity. Cell viability analysis showed that ES20 (92.53 ± 2.57%) was comparable to ES0 (94.01 ± 2.01%) (p-value > 0.05, Fig. 2E). Nanoparticle tracking analysis (NTA) confirmed that sEVs from ES20 and ES0 had similar particle sizes (125.73 ± 16.11 nm vs. 131.77 ± 0.67 nm, respectively) and particle concentrations (64.13×10^6 ± 22.73×10^6 vs. 83.33×10^6 ± 9.61×10^6 particles/mL, respectively) (p-value > 0.05, Fig. 2F and G).

The ES20 protocol was validated as non-cytotoxic, maintaining cell morphology, viability, and sEV characteristics within a 60-mm culture dish using a DC power supply of 900 mV. Consequently, ES20 was implemented in the sequential stimulation experiments.

Sequential stimulation affects core genotypes relating to sEV production by cAD-MSCs without cytotoxicity

To enhance sEV production by cAD-MSCs, three biophysical stimulation protocols were employed: (1) low-oxygen gas preconditioning (IVFG; 5% O_2, 6% CO_2, balance N_2) using in vitro fertilization gas, (2) electrical stimulation at 20 mV/mm (ES20), and (3) the combination of IVFG and ES20 termed sequential stimulation (IVES). The experimental platforms are illustrated in Fig. 3B, with protocols applied after cell maintenance in the in-house sEV-collecting medium (VSCBIC-3). sEVs were collected from Day 1 (D1) and pooled Day 2 + Day 3 (D2D3) media for subsequent analyses.

As shown in Fig. 3C, cAD-MSCs subjected to IVFG, ES20, and IVES maintained fibroblastic morphology similar to controls (CTRL) on both D1 and D2D3. Cell viability analysis revealed that IVFG tended to increase viable cell counts at D1 (1.33 ± 0.41 AU) and D2D3 (1.38 ± 0.30 AU), while IVES exhibited similar trends, particularly at D2D3 (1.13 ± 0.36 AU). In contrast, ES20 caused a reduction in viable cell count at D2D3 (0.56 ± 0.12 AU, Fig. 3D). Although no significant differences in cytotoxicity were observed among groups, IVES consistently maintained higher cell viability across all time points, demonstrating superior biocompatibility compared to ES20.

RT-qPCR analysis of mRNA markers related to cellular stimulation and sEV production is summarized in Fig. 3E. IVES significantly upregulated the hypoxia activation marker *Hif1a* at D1 (1.88 ± 0.59 AU), whereas IVFG downregulated its expression (0.55 ± 0.13 AU). At D2D3, IVES maintained a trend of *Hif1a* upregulation (1.51 ± 0.71 AU), whereas IVFG and ES20 were comparable to CTRL. For the calcium homeostasis marker *Hsp90b1*, all stimulations showed trends of upregulation at D1, with IVFG displaying the highest expression (1.18 ± 0.03 AU). However, significant downregulation of *Hsp90b1* was observed in IVFG at D2D3 (0.86 ± 0.04 AU). For sEV biogenesis markers, *Rab27b* expression remained comparable across groups except for significant downregulation with ES20 at D1 (0.47 ± 0.25 AU). IVES exhibited the highest trend of *Syntenin-1* upregulation at D1 (1.36 ± 0.18 AU), highlighting its potential role in enhancing sEV production. At D2D3, significant

(See figure on next page.)

Fig. 3 Establishment of sequential stimulation of cAD-MSCs for small extracellular vesicle (sEV) production. **A** The schematic diagram demonstrates the protocol for sequential stimulation of cAD-MSCs, as well as the subsequent collection and purification of sEVs. **B** While CTRL was incubated under normal condition, IVFG was conducted by flowing through with the in vitro fertilization gas (5% O_2). ES20 was done by applying a direct current at 20 mV/mm through the platinum electrodes. For IVES, cAD-MSCs underwent IVFG and ES20 consecutively. **C** Morphological appearances of cAD-MSCs before conditioned medium collection were revealed by a phase-contrast microscope at 200X magnification. The scale bars represent 200 µm. **D** Viable cells were counted by trypan blue exclusion assay. The fold change in viable cell count was obtained by CTRL normalization. **E** Expression of mRNA makers for hypoxia activation (*Hif1a*), calcium homeostasis (*Hsp90b1*), exosome biogenesis (*Syntenin-1*) and endolysosomal trafficking (*Rab27b*) were analyzed via RT-qPCR. The relative mRNA expression was determined by normalization with the reference gene (*Gapdh*). The fold change in mRNA expression was calculated by normalization with *Gapdh* and the control condition (CTRL). **F** Pearson's correlation matrix of the relative mRNA expressions demonstrates the data distribution as a density plot (diagonal) and the correlation between genes as a pairwise scatter plot (lower diagonal). The linear regression curve was visualized along with a grey region of 95% confidence interval. The Pearson's correlation coefficient (R) was annotated with statistical significance symbol (*; p-value ≤ 0.05, **; p-value ≤ 0.01). In boxplots, mean values of each group were annotated at the bottom, and global statistics were stated at the top. The bars indicate pairwise comparisons (ns; no significance or p-value > 0.05, *; p-value ≤ 0.05). Abbreviation: CTRL; control condition, IVFG; in vitro fertilization gas pre-conditioning, ES20; electrical stimulation at 20 mV/mm, IVES; sequential stimulation of IVGF and ES20. D1; sEV sample from Day1 collection, D2D3; pooled sEV sample from Day2 and Day3 collections, and AU; arbitrary unit

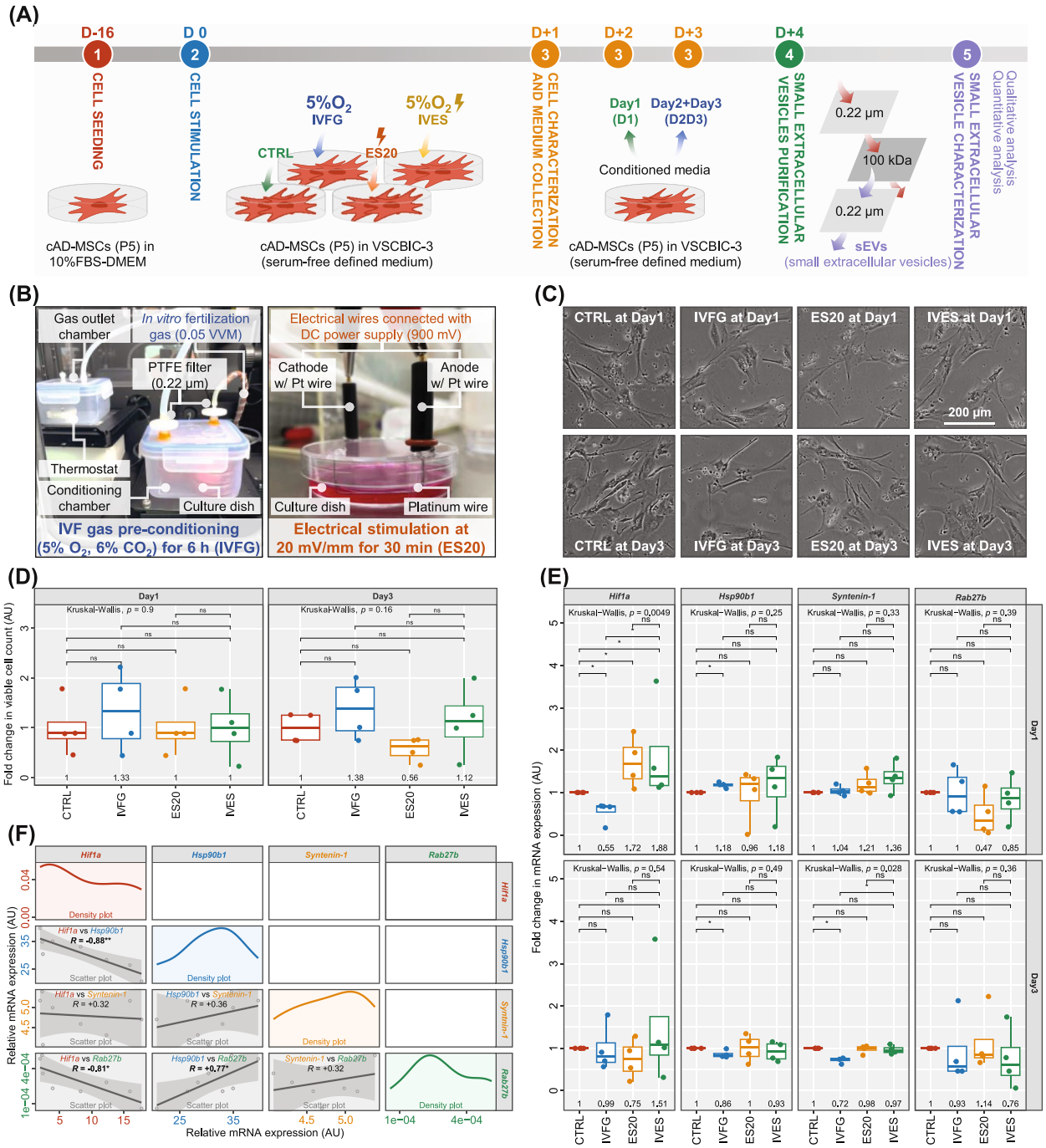

Fig. 3 (See legend on previous page.)

downregulation of *Syntenin-1* was observed with IVFG (0.72 ± 0.03 AU).

Correlation analysis using Pearson's correlation matrix (Fig. 3F) revealed significant relationships between markers. Negative correlations were found between *Hif1a* vs. *Hsp90b1* ($R = -0.88$, p-value ≤ 0.01) and *Hif1a* vs. *Rab27b* ($R = -0.81$, p-value ≤ 0.05), while a positive correlation was observed between *Hsp90b1* vs. *Rab27b* ($R = +0.77$, p-value ≤ 0.05). IVES demonstrated synergistic effects by upregulating *Hif1a* and maintaining consistent *Hsp90b1* expression across time points. The highest trend of *Syntenin-1* upregulation further supports IVES's role in promoting sEV biogenesis.

In summary, sequential stimulation using IVES demonstrated non-cytotoxicity while effectively modulating key genotypic markers associated with sEV production. Correlation analysis revealed positive interactions between mRNA markers of cellular stimulation and sEV production pathways, emphasizing the potential of IVES for optimizing sEV production.

Sequential stimulation (IVES) of cAD-MSCs showed trends toward improved sEV stability and quality profiles

The novel IVES technique for sequential stimulation of cAD-MSCs demonstrated significant benefits in enhancing sEV stability and quality profiles, particularly in the D2D3 sample pool. Morphological analysis using TEM confirmed that sEVs from all stimulations displayed the characteristic cup-shaped vesicle structure, with particle sizes ranging from 50 to 300 nm (Fig. 4A) [27]. Flow cytometry analysis, using a canine-specific anti-CD9 antibody, employed gating set below the peak area of violet side scatter (Violet SSC-A) of 300-nm polystyrene beads ($< 10^5$ AU), with the sEV population subsequently gated for CD9 positivity. Isotype control plots (IgG1 kappa) confirmed the alignment of CD9-positive populations diagonally with the Pacific Blue-conjugated CD9 channel (CD9-PB450-A) and Violet SSC-A (Fig. 4B) [28]. While D1 samples showed reduced CD9 positivity compared to the control, D2D3 samples exhibited an increase in this parameter, suggesting their suitability for sEV collection (Fig. 4C).

Zeta-potential analysis highlighted the impact of IVES on sEV surface charge. While CTRL sEVs had a zeta potential of -22.37 ± 0.26 mV, IVES stimulation produced sEVs with a more stable negative charge of -23.97 ± 0.58 mV in the D2D3 pool, indicating enhanced stability and reduced aggregation risk (Fig. 4D) [29]. Quantitative characterization using nanoparticle tracking analysis (NTA) confirmed that sEVs exhibited a size range of 50–300 nm, with scattered light represented

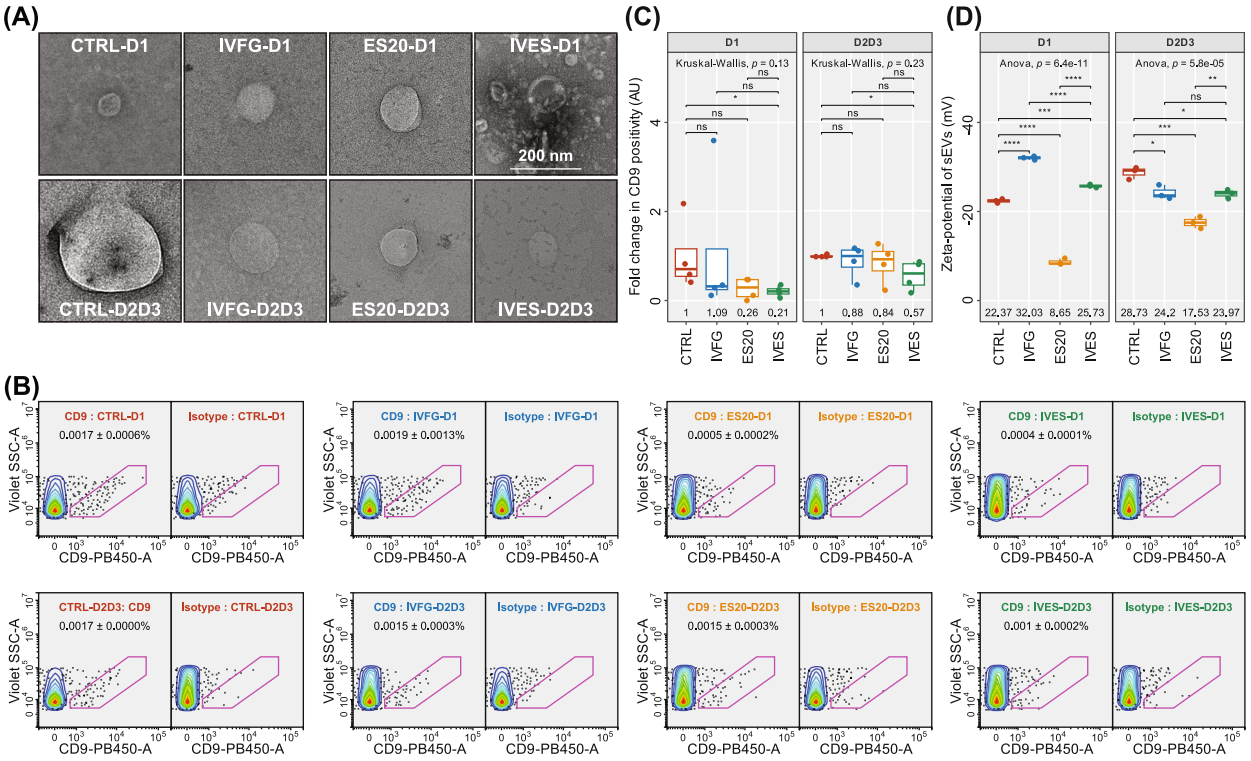

Fig. 4 Characterization of small extracellular vesicles (sEVs) isolated from conditioned medium of cAD-MSCs after sequential stimulation. **A** Transmission electron microscope at 200 kV was used to observe a cup-shape morphology of sEVs stained with uranyl acetate. The scale bar represents 200 nm. **B** Exosomal surface marker CD9 of sEV samples was determined by nanoscale flow cytometry. The isotype control aided in gating for CD9-positive particles in the pink region. **C** The fold change in CD9 positivity was estimated by normalization with CTRL. **D** Stability of sEV sample was implied from the zeta-potential. It was characterized by using a Zetasizer Nano ZS. In boxplots, mean values of each group were annotated at the bottom, and global statistics were stated at the top. The bars indicate pairwise comparisons (ns; no significance or *p*-value > 0.05, *; *p*-value ≤ 0.05, **; *p*-value ≤ 0.01, ***; *p*-value ≤ 0.001, ****; *p*-value ≤ 0.0001). Abbreviation: CTRL; control condition, IVFG; in vitro fertilization gas pre-conditioning, ES20; electrical stimulation at 20 mV/mm, IVES; sequential stimulation of IVGF and ES20. D1; sEV sample from Day1 collection, D2D3; pooled sEV sample from Day2 and Day3 collections, AU; arbitrary unit, Violet SSC-A; peak area of violet side scatter, and CD9-PB450-A; peak area of Pacific Blue-conjugated CD9 at 450 nm channel

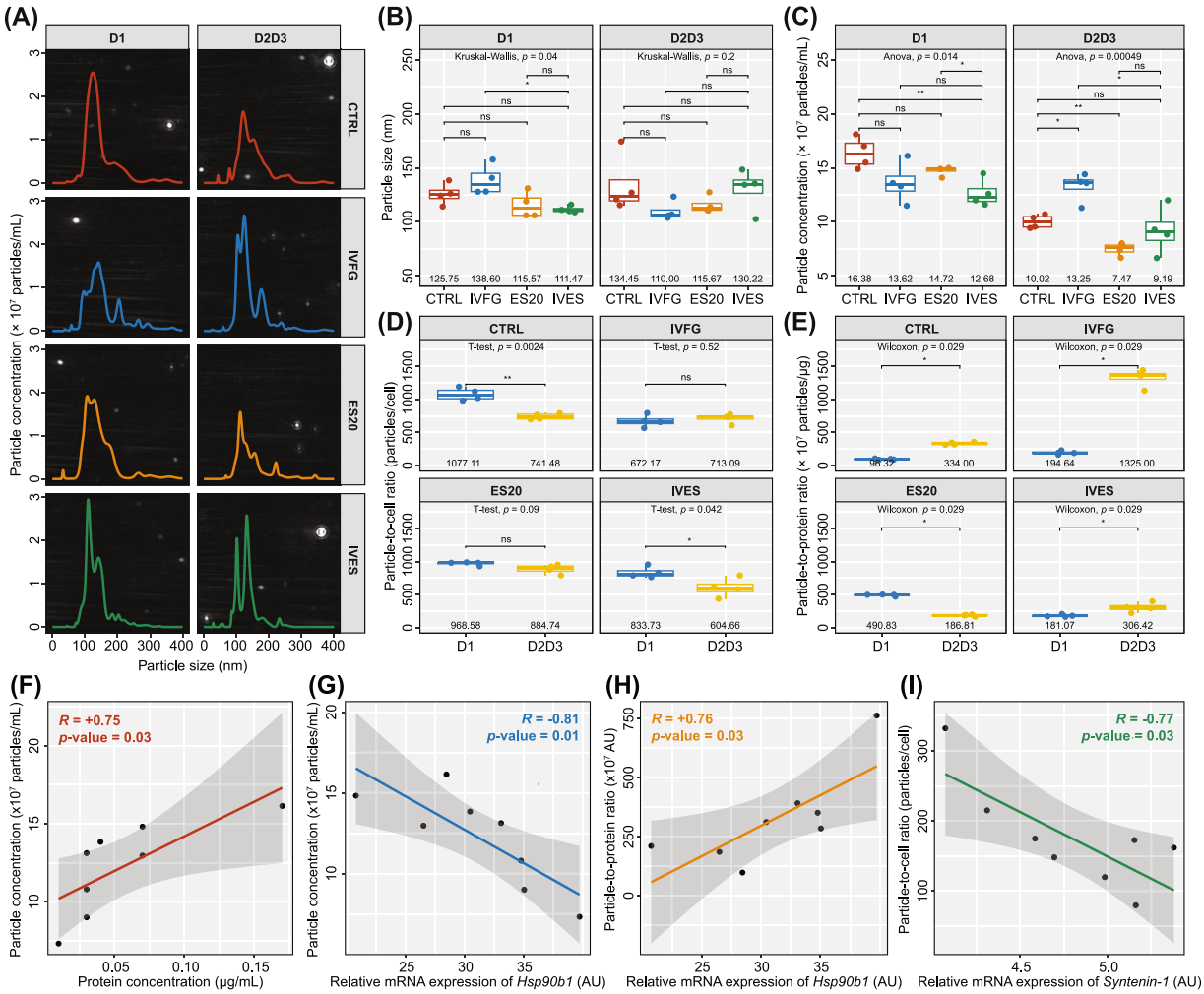

Fig. 5 Quantitative analysis and quality profiles of small extracellular vesicles (sEVs) isolated from conditioned medium of cAD-MSCs after sequential stimulation. **A** Nanoparticle tracking analysis (NTA) was performed by recording the videos of the laser scattering particles moving under Brownian motion. The line plots visualize the particle size and distribution of representative sEV samples, in which the laser scattering particles, bright spots, were depicted as a background image. **B** The particle size, modal hydrodynamic diameter, was estimated by tracking the particles in the video based on Stokes-Einstein equation. **C** The particle concentration was calculated from the particle number in the field of view from the video. **D** The particle-to-cell ratio was reported as a production yield of sEVs from cAD-MSCs. **E** The particle-to-protein ratio was considered as a purity of sEV sample. For Pearson's correlation analysis, the linear regression curve was visualized along with a grey region of 95% confidence interval, in which the coefficient (*R*) the *p*-value were also annotated. The correlations of the particle concentration and the protein concentration (**F**), the particle concentration and the relative mRNA expression of *Hsp90b1* (**G**), the particle-to-protein ratio and the relative mRNA expression of *Hsp90b1* (**H**), and the particle-to-cell ratio and the relative mRNA expression of *Syntenin-1* (**I**) were considered. In boxplots, mean values of each group were annotated at the bottom, and global statistics were stated at the top. The bars indicate pairwise comparisons (ns; no significance or *p*-value > 0.05, *; *p*-value ≤ 0.05, **; *p*-value ≤ 0.01, ***; *p*-value ≤ 0.001, ****; *p*-value ≤ 0.0001). Abbreviation: CTRL; control condition, IVFG; in vitro fertilization gas pre-conditioning, ES20; electrical stimulation at 20 mV/mm, IVES; sequential stimulation of IVGF and ES20. D1; sEV sample from Day1 collection, and D2D3; pooled sEV sample from Day2 and Day3 collections

in the background images of the line plots in Fig. 5A. IVES samples showed consistent quality and size distribution across both D1 and D2D3 pools, indicating the reliability of this approach. Particle concentration and particle-to-cell ratios were comparable across all groups, with IVES demonstrating efficient production during both collection periods (Fig. 5C and D). Furthermore, particle-to-protein ratios indicated that prolonged collection in the D2D3 pool improved sEV purity, with IVES achieving optimal outcomes (Fig. 5E).

Correlation analysis of key factors influencing sEV quality and production further supported the benefits of IVES. A strong positive correlation was observed between particle concentration and protein

concentration ($R = +0.75$, p-value ≤ 0.05) (Fig. 5F). Interestingly, *Hsp90b1* expression was negatively correlated with particle concentration ($R = -0.81$, p-value ≤ 0.01) but positively correlated with particle-to-protein ratio ($R = +0.76$, p-value ≤ 0.05) (Fig. 5G and H). Additionally, a negative correlation was noted between particle-to-cell ratio and *Syntenin-1* expression ($R = -0.77$, p-value ≤ 0.05) (Fig. 5I). These findings highlight the role of IVES in modulating genotypic factors critical for enhancing sEV quality and stability.

Taken together, the IVES technique demonstrated superior performance in enhancing sEV stability, purity, and quality, particularly in the D2D3 collection period. Correlation analysis confirmed the synergistic effects of IVES in optimizing key production pathways, supporting its potential as a robust platform for producing high-quality sEVs suitable for clinical and industrial applications.

sEVs derived from sequential stimulation of cAD-MSCs exert anti-inflammatory activity in LPS-induced macrophage model

To explore the clinical potential of sEVs, their anti-inflammatory and pro-proliferative activities were evaluated using a lipopolysaccharide (LPS)-induced macrophage model. RAW264.7 murine macrophages served as representative inflammatory cells, with the experimental design summarized in Fig. 6A. Two aspects of sEV bioactivity were analyzed: (1) anti-inflammatory effects on LPS-induced macrophages (M1 polarization model) and (2) pro-proliferative effects on non-LPS-induced macrophages (M0 macrophage model) (Fig. 6B).

For the M1 macrophage polarization model, nitric oxide inhibition (NOI) was assessed as a measure of anti-inflammatory activity. sEVs derived from IVES stimulation exhibited superior anti-inflammatory activity compared to other groups, with NOI values of $20.03 \pm 6.79\%$ (D1 sample) and $31.98 \pm 6.64\%$ (D2D3 pool), outperforming CTRL and other stimulation groups (Fig. 6C). Normalizing the activity to CTRL demonstrated that sEVs from the IVES group, particularly D2D3 samples, had the highest relative anti-inflammatory activity (Fig. 6D). Morphological observations further supported these findings, as sEVs from IVES maintained the unpolarized (M0) morphology of the majority of RAW264.7 cells upon LPS stimulation, similar to the effect of dexamethasone (DEXA) (Fig. 6E). The colorimetric Griess assay confirmed that sEVs from IVES reduced NO production, changing the magenta color from LPS-stimulated cells (PBS + LPS+) to orange, comparable to DEXA ($59.04 \pm 5.46\%$) (Fig. 6F). Notably, sEVs from IVES stimulation reduced NO production by $31.98 \pm 6.64\%$.

For the M0 macrophage model, baseline NO production by non-LPS-stimulated RAW264.7 cells was reduced by sEVs from all stimulation groups, matching the effects of DEXA (Fig. 6G). Additionally, sEVs from IVES enhanced macrophage proliferation compared to CTRL (Fig. 6H), indicating potential immunomodulatory effects. These findings suggest that IVES-derived sEVs effectively regulate baseline NO production and enhance macrophage population growth.

Collectively, sEVs generated via IVES stimulation demonstrated powerful anti-inflammatory effects in the LPS-induced macrophage model and immunomodulatory activity in the M0 macrophage platform, supporting their potential for therapeutic applications.

Discussion

Over the past decade, small extracellular vesicles (sEVs) have gained significant attention for their therapeutic potential, particularly in veterinary research [5, 7, 30–33]. Thus, we refined the protocol to enhance the production of anti-inflammatory sEVs from canine adipose-derived mesenchymal stem cells (cAD-MSCs), given the growing interest in utilizing these vesicles for medical interventions. According to our previous reports [34, 35], cAD-MSCs underwent isolation and expansion. Their characterization followed to the International Society for Cellular Therapy (ISCT) standards [36], exhibiting a fibroblast-like morphology and adherence to a plastic tissue culture dish. Furthermore, the cells met MSC criteria by expressing surface markers of an adhesion marker CD90, a hyaluronate receptor CD44, and an integrin beta 1 CD29 while lacking a hematopoietic stem cell marker CD45 [36–39]. Expression of stemness-associated markers *Oct4* and *Rex1*, and a proliferation marker *Ki-67* indicated multi-potent and proliferative properties [34, 35, 40–43]. In addition, enzymatic subculture confirmed their proliferation capacities with a consistent population doubling time up to passage 5. The isolated cells demonstrated adipogenic, osteogenic, and chondrogenic differentiation capabilities, aligning with earlier research [34, 41, 43–49], affirming the potential and the homogeneity of cAD-MSCs for sEV production. The comprehensive characterization and functional validation make the isolated cAD-MSCs as a reliable source for sEV production.

The absence of exogenous substances in biophysical stimulation mitigates the risk of unintended contamination, allowing precise modulation of cellular activities [12]. In this study, we introduce a sequential biophysical stimulation approach to modulate cAD-MSCs for sEV production, combining IVF gas preconditioning and DC electrical stimulation. While prior studies noted the influence of DC electrical stimulations on MSC behaviors [12, 13, 20–24], optimization is crucial due to distinct

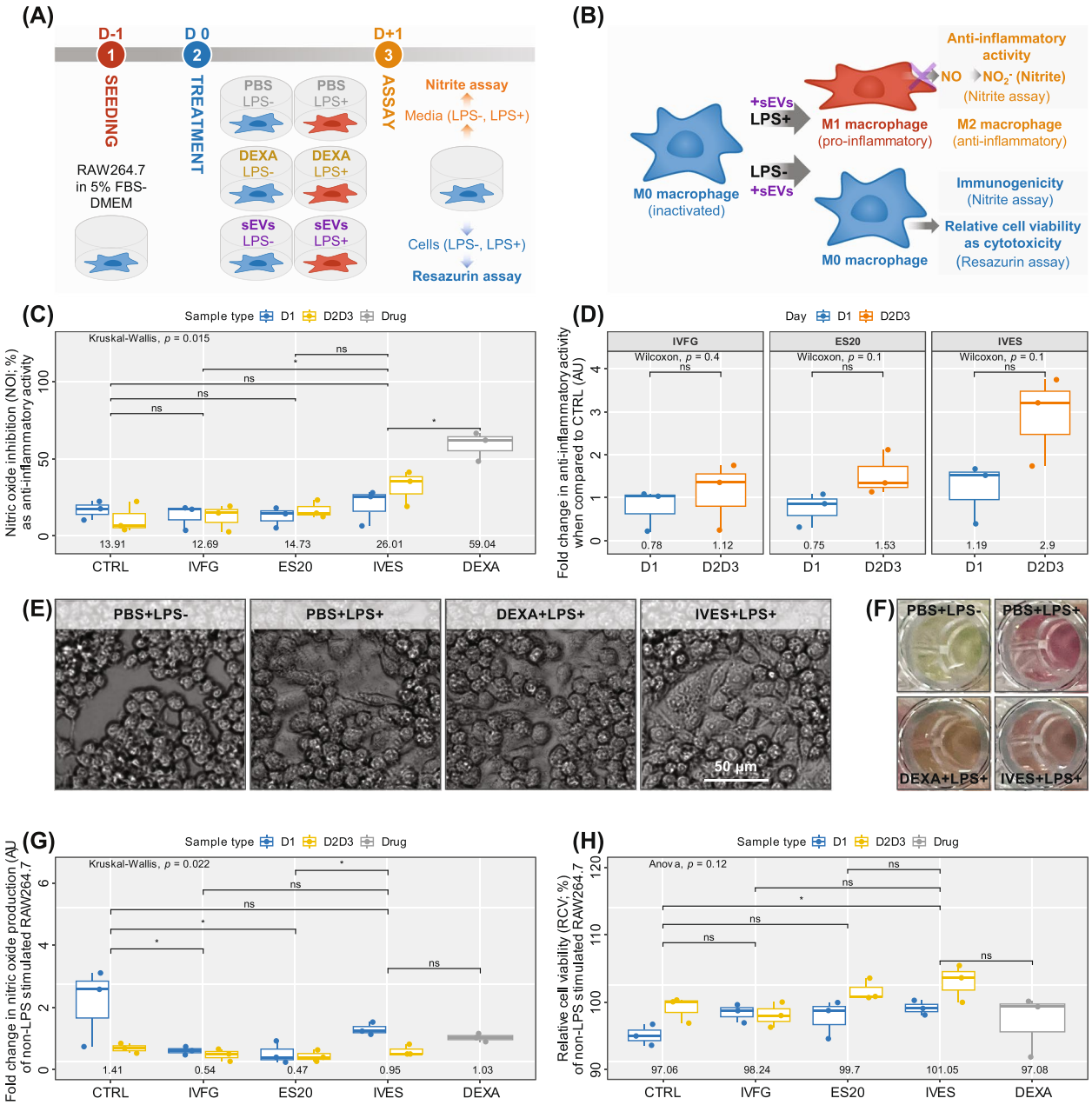

Fig. 6 Anti-inflammatory activity of small extracellular vesicles (sEVs) isolated from conditioned medium of cAD-MSCs after sequential stimulation. The schematic diagram represents the protocol (**A**) and the concept (**B**) for determination of anti-inflammatory activity of sEVs using lipopolysaccharide (LPS)-induced macrophage model. **C** Nitric oxide (NO) inhibition determined from nitrite assay indicates the anti-inflammatory activity. **D** Fold change in anti-inflammatory activity was normalized with CTRL. **E** The microscopic appearance of RAW264.7 in the representative wells after co-incubation was observed under 200X magnification. The scale bar represents 50 µm. **F** The appearance of the representative conditioned media underwent Griess reaction in nitrite assay. **G** Relative cell viability of non-LPS stimulated RAW264.7 evaluated from resazurin assay was considered as cytotoxicity of sEV sample. **H** Fold change in NO production of non-LPS stimulated RAW264.7 was implied for immunogenicity of sEV sample. In boxplots, mean values of each group were annotated at the bottom, and global statistics were stated at the top. The bars indicate pairwise comparisons (ns; no significance or *p*-value > 0.05, *; *p*-value ≤ 0.05). Abbreviation: CTRL; control condition, IVFG; in vitro fertilization gas pre-conditioning, ES20; electrical stimulation at 20 mV/mm, IVES; sequential stimulation of IVGF and ES20. D1; sEV sample from Day1 collection, D2D3; pooled sEV sample from Day2 and Day3 collections, LPS-; non-LPS-induced condition, LPS+; LPS-induced condition, PBS; phosphate buffered saline, DEXA; dexamethasone, and AU; arbitrary unit

experimental setups. Utilizing the in-house sEV-collecting medium (VSCBIC-3), our DC electrical stimulation platform was successfully established without cytotoxic effects against cAD-MSCs. This platform could produce sEVs up to 8×10^7 particles/mL as indicated by nanoparticle tracking analysis (NTA). In addition, the modal size was smaller than 150 nm, suggesting the major population of nanoparticles was sEVs [50]. To generate the electric field, we employed a 45-mm spaced electrode lid with platinum wire electrodes, fitting our in vitro experiment with 5 mL conditioned medium. This scale aligned with sEV purification involving syringe filters for microfiltration and centrifugal filters for ultrafiltration. Platinum electrodes, chosen for their inert nature and biocompatibility [13, 51], outperformed silver/silver chloride and carbon electrodes in durability and customizability, despite higher costs. Bubbles generated during DC electrical stimulation suggested electrolysis in the medium, possibly release oxygen gas at the anode and hydrogen gas at the cathode [26, 52]. To minimize stress, we set the stimulation time to 30 min, different from longer durations in other [13, 23, 24].

Our screening experiment unveiled the delicate balance between stimulation effectiveness and cell integrity, with ES20 emerging as non-cytotoxic, while ES100 led to adverse effects, including morphological alterations, detachment, and lysis. The results suggest that ES100 induces acute cytotoxicity, possibly linked to electrophoretic effects or electrochemical reactions generating hydrogen peroxide as a faradaic by-product [25]. The pH changes under the electrodes during stimulation are stabilized by the buoyancy effect induced by gas bubbles, in which treating for 2 h did not alter the pH of the culture media [25, 53]. By using 22-mm spaced platinum electrodes in the previous study [13], the DC electrical stimulation of rat MSCs for 1 h revealed that 200 mV/mm (4,400 mV) affected cellular disintegration, while 100 mV/mm (2,200 mV) was non-cytotoxic. Taken together, our findings supported that cytotoxic voltage for in vitro DC electrical stimulation exceeds 4,400 mV, while biocompatible voltage is below 2,200 mV, supporting the safety of our voltage applied for the sequential stimulation.

In a pioneering achievement, we have introduced a sequential stimulation method, termed IVES, for the enhanced anti-inflammatory sEVs produced by cAD-MSCs. IVES combines two distinct approaches: low-oxygen gas mixture preconditioning using in vitro fertilization gas (IVFG) under 0.005 VVM for 6 h and direct current electrical stimulation at 20 mV/mm for 30 min (ES20). In the prior investigation, the combined use of cyclic strain and electrical stimulation demonstrated a significant enhancement in the neural differentiation of bone marrow-derived mesenchymal stem cells [10]. Our novel technique not only serves as a robust and flexible tool for manipulating cellular processes but also exhibits substantial potential for a wide range of scientific and therapeutic applications. The biocompatibility of the stimulations, as confirmed by cell morphology and viability assessments, highlights the safety of this approach. After purification, the observations of cup-shaped vesicles under TEM provided evidence for the existence of sEVs. The obtaining sEVs ranged from 50 to 300 nm in size was confirmed by TEM and NTA. It proves that our purification process successfully eliminated apoptotic bodies, microvesicles, and large particles by conducting dead-end microfiltration with a 0.22-μm syringe filter [54]. Following that, ultrafiltration using a 100-kDa centrifugal filter effectively retained sEVs while eliminating soluble factors, such as small molecular weight proteins, leading to a remarkable sEV purity [55]. Our purification procedure yielded approximately 1.8 mL of the sterilized sEV sample. The particle-to-protein ratios exhibited a significant range, ranging from 9.63×10^8 to 1.33×10^{10} particles/μg. This performance surpassed the particle-to-protein ratios of sEV samples generated from human adipose-derived MSCs under static and 3D cultures, which were only 9.88×10^8 and 3.40×10^8 particles/μg, respectively [56].

Unexpectedly, the expression of exosomal surface marker CD9 was absent in our finding, but the previous work reported the presence of this marker in sEVs produced from cAD-MSCs [6]. However, CD9 and CD63 tetraspanins in EVs are not involved in cargo delivery process [57]. While the size range of 50–300 nm is commonly associated with exosomes, the lack of well-defined biomarkers and the size overlap among different vesicle types make it challenging to discriminate between them solely based on size [58]. According to the modal sizes determined were less than 150 nm, these nanoparticles were solely considered as small extracellular vesicles or sEVs, originating from endosomal or non-endosomal pathways [50]. The observed positive correlation between particle concentration and protein concentration ($R = +0.75$) suggests the production of sEVs from cAD-MSCs. These vesicles, which are constructed form phospholipid bilayers, contain transmembrane proteins and protein cargos [59]. This correlation highlights the interplay between the structural components of sEVs and their protein content, shedding light on the mechanisms involved in their biogenesis and cargo packaging.

In our experiment, individual stimulations exerted distinct effects on gene expressions in cAD-MSCs, while IVES demonstrated a unique combination of characteristics from IVFG and ES20. In this finding, IVFG particularly upregulated *Hsp90b1* expression, indicating calcium homeostasis stabilization [60, 61], but concurrently

downregulated *Hif1a*, associated with hypoxia activation [18]. To the best of our knowledge, the inverse relationship between the expression of *Hsp90b1* and *Hif1a* in cAD-MSCs was spotted for the first time according to Pearson's correlation analysis ($R = -0.88$). It is notable that despite the utilization of in vitro fertilization gas (5% O_2, 6% CO_2) to create low oxygen conditions for 6 h [15, 18], *Hif1a* expression in IVFG was not upregulated. Serum deprivation induced by VSCBIC-3 in this study may be responsible for induction of *Hif1a* expression in the control condition [62]. Therefore, reoxygenation for 18 h post-preconditioning might suppress hypoxia signaling in IVFG. This observation contrasts with an earlier study where exposure to hypoxia/reoxygenation did not alter *Hif1a* expression in MSCs [63], emphasizing the influence of experimental conditions. On Day 3, *Hsp90b1* notably decreased in IVFG, aligning with increased sEV concentration ($R = +0.88$) and reduced sEV purity ($R = +0.76$). Remarkably, the particle-to-cell ratio held steady, while the particle-to-protein ratio significantly rose, mirroring IVES outcomes. *Syntenin-1* downregulation, correlated negatively with sEV purity ($R = -0.77$), supports this trend. The correlation ($R = +0.77$) between *Hsp90b1* and *Rab27b* expressions suggests sEV yield elevation independently of the endosomal sorting complexes required for transport (ESCRT) pathway and endolysosomal trafficking, unlike in cancer cells [64]. cAD-MSCs might use an ESCRT-independent pathway, possibly the ceramide pathway. In the ceramide-based sphingomyelinase (SMase) pathway, sphingomyelin hydrolysis yields phosphorylcoline and ceramide [65]. Beneficially, our results align with the previous study showing that disrupting endolysosomal trafficking boosts exosome release while preserving their regenerative bioactivity [66].

Outstandingly, ES20 and IVES upregulated *Hif1a* expression. Despite various ion channels being activated by biophysical stimuli [67], the authors propose that undergoing direct electrical stimulation in acidic electrolytes might generate hydrogen peroxide (H_2O_2) as a faradaic by-product, eliminating dissolved oxygen [25, 68]. Additionally, this oxidative stress potentially induced adaptation mechanisms, resulting in the upregulation of *Hif1a* [69, 70]. Electrical stimulation can drive ATP/Ca^{2+} oscillations, contributing to TGF-β signaling [12]. However, TGF-β1 treatment boosts HIF-1α and HIF-2α expression in normoxia without affecting mRNA levels or protein degradation rates. This suggests that TGF-β1 impacts HIF-1α/2α expression primarily at the translation level [71]. Surprisingly, ES20 led to a considerable decrease in the zeta potential of sEVs (−8.65 mV). This phenomenon might be attributed to the electrophoretic effect that drawn negative-charged vesicles to deposit at the anode, leading to a significant reduction in zeta potential. The zeta potential reflects the surface charge of particles, and a decline in negativity indicates a shift toward reduced stability [29, 72]. The reduced negativity below −15 mV caused by ES20 suggests that the electrostatic repulsion between sEVs is diminished, making them more prone to aggregation [29]. Surprisingly, the adverse effect was resolved by undergoing IVFG to produce more negative vesicles (−32.03 mV) before conducting ES20. It elevated the negativity of the sEV surface to −25.73 mV.

The reproducibility and scalability of the IVES technique are crucial for translating sEV production into clinical and industrial applications. In 2D culture systems, multi-layer platforms like CellSTACK and HYPERFlask facilitate large-scale cell expansion, integrating uniform low-oxygen preconditioning and electrode grids for electrical stimulation to ensure process consistency. For 3D cultures, microcarrier-based systems in spinner flasks, wave bioreactors, and stirred-tank bioreactors support high-density cell cultures, offering precise control over oxygen levels, shear forces, and nutrient delivery [73]. Electrical stimulation in 3D systems can be implemented by embedding electrode arrays within bioreactor chambers, though optimizing electrical fields without impacting cell growth remains a challenge in larger platforms. Hollow fiber-based bioreactors enhance scalability by allowing compartmentalized nutrient and gas exchange, supporting continuous culture and efficient sEV harvesting. Microfluidic platforms further advance scalability by providing tightly controlled microenvironments for replicating IVES conditions at high throughput, while enabling seamless integration with downstream processes [74]. Real-time monitoring systems for oxygen concentration, pH, and electrical stimulation are vital across all platforms to maintain consistency. Scalable sEV harvesting techniques, including tangential flow filtration and continuous centrifugation, enhance the efficiency and reproducibility of IVES processes [75]. Together, these innovations position IVES as a versatile, reproducible, and scalable method to meet the growing demand for therapeutic and industrial sEV production.

Throughout this study, the innovative sequential stimulation has reshaped our understanding of cellular responses. This research not only optimizes a method for sEV production but also investigates their function in anti-inflammation. The anti-inflammatory assessment of cAD-MSC-derived sEVs employed a lipopolysaccharide (LPS)-induced RAW264.7 macrophage model at passage 8. A concentration of 1,000 ng/mL LPS induced pro-inflammatory macrophages (M1 phenotype) from inactivated macrophages (M0 phenotype) seeded at 1.0×10^5 cells/well on a 96-well plate. This condition facilitated

optimal nitric oxide (NO) release, measured colorimetrically through a nitrite assay. The absorbance at 570 nm exceeded 0.10, indicating substantial NO production by inducible nitric oxide synthase (iNOS). Nitrite, formed in the culture media, was quantified via the Griess reaction, yielding a magenta solution under acidic conditions [76–78]. In the previous study [76], a LPS concentration of 10 ng/mL stimulated RAW264.7 cells seeded at a density of 2.0×10^4 cells/well. Their sEV dose of 1.0×10^9 particles/mL, normalized as 5.0×10^4 particles/seeding cell, resulted in NO production inhibition ranging from 50 to 90%, leading to polarization toward anti-inflammatory macrophages (M2 phenotype). In our experiment, a dose of 1.5×10^8 particles/mL was deemed suitable for assessing anti-inflammatory activity. Among the sEV samples, IVES-D2D3 exhibited the highest inhibition at 31.98%. The lower NO inhibition (NOI) might be attributed to the reduced normalized dose of 1.5×10^3 particles/seeding cell. Nonetheless, the use of 1.25 µg/mL DEXA in our study demonstrated an inhibition of 59.04%, closely aligning with the 60% inhibition reported for 1.00 µg/mL DEXA in their study.

Developing upon prior studies [76, 77], our anti-inflammatory activity determination protocol incorporated the resazurin assay to evaluate cytotoxicity based on cellular activity. The relative cell viability (RCV) results indicate that sEVs from cAD-MSCs, when incubated with RAW264.7 macrophages, exhibit non-cytotoxic effects, with values surpassing 70% [77]. Moreover, IVES significantly increased RCV in non-LPS-induced RAW264.7 cells compared to the control (CTRL). While lacking statistical correlation with NOI (Fig. S1), the authors observe a potential link between superior anti-inflammatory activity and increased cell viability or related cellular mechanisms. This observation is reinforced by the RCV comparison between LPS-stimulated and non-stimulated cells, showing higher values in stimulated cells (Fig. S2). Notably, pro-inflammatory macrophages predominantly utilize glycolysis, accompanied by compromised tricarboxylic acid cycle activity and mitochondrial oxidative phosphorylation (OXPHOS). In contrast, anti-inflammatory macrophages demonstrate a greater reliance on mitochondrial OXPHOS [79].

While co-incubating sEVs from IVES resulted in a substantial reduction in NO release by up to 26%, other conditions demonstrated inhibitions below 15%. This distinctive response suggests that the sequential stimulation method employed in IVES might induce the synthesis of diverse sEV cargo, encompassing lipids, proteins, and nucleotides [80]. The complexity of the mechanisms underlying the paracrine action of sEVs has hindered a comprehensive understanding thus far. sEVs might fuse with the cell membranes or binding to membrane proteins of recipient cells. It might alleviate inflammation by reshaping macrophage polarization towards an M2 phenotype through the inhibition of tumor necrosis factor receptor-associated factor 1 (TRAF1). This leads to the suppression of pro-inflammatory factor expression via modulation of the MAPK and NF-κB signaling pathways [81, 82]. It is conceivable that sEVs from sequential stimulation may carry CD73 on their surface. CD73 activity could shift from an ATP-driven pro-inflammatory state to an anti-inflammatory environment induced by adenosine, influencing immunosuppression (68–70). To validate these hypotheses, future work should include cellular uptake assays, TRAF1 pathway modulation, and CD73 activity assessments. In our study, the fold change in anti-inflammatory activity tended to increase in later sEV collections but was not statistically significant among stimulation techniques, encouraging the benefit of prolonged conditioned medium collection. According to the stem cells is substantially limited for large-scale production, these conditioned media could be combined to improve the production yield before purification in the further work. Concurrently, our protocol measured the fold change in NO release from non-stimulated cells to assess their immunogenicity [83]. The findings indicated that IVFG and ES20 significantly decreased immunogenicity compared to the control (CTRL), resulting in the production of sEVs with low immunogenic characteristics, particularly evident in IVES.

The potential clinical applications of small extracellular vesicles (sEVs) derived from canine adipose-derived mesenchymal stem cells (cAD-MSCs) in veterinary medicine are extensive, primarily due to their anti-inflammatory and immunomodulatory properties [84, 85]. These vesicles show promise in treating chronic inflammatory diseases such as canine arthritis, where their ability to modulate immune responses and promote tissue repair could alleviate pain and improve joint function [31, 86]. Similarly, in cases of inflammatory bowel disease, sEVs may help restore intestinal homeostasis by reducing inflammation and supporting mucosal healing [87, 88]. For atopic dermatitis, a common skin condition in dogs, systemic or localized administration of sEVs could suppress inflammatory pathways, alleviated skin bacterial dysbiosis, and accelerate skin barrier restoration [89, 90]. Moreover, sEVs have demonstrated potential in wound healing applications, where their bioactive cargo could promote cellular proliferation, angiogenesis, and matrix remodeling, expediting the repair of chronic or acute wounds [90–92]. Despite these promising applications, challenges remain in developing stable formulations suitable for various delivery methods. For instance, injectable

formulations require long-term stability and controlled release, while topical or localized delivery systems must overcome barriers such as absorption efficiency and targeted bioavailability [92–94]. Addressing these formulation challenges is critical for maximizing the therapeutic potential of sEVs in veterinary medicine.

Limitations of this study primarily arise from the small sample size, which may restrict the generalizability of the findings. Variability in donor-derived cAD-MSCs, including differences in genetic background, health status, and tissue sources, presents additional challenges, potentially impacting the reproducibility and robustness of the observed outcomes. While the study highlights the promise of IVES for enhancing sEV production and quality, translating these findings into clinical applications remains complex. Key challenges include scaling up sEV production to meet clinical demands while ensuring consistent quality, navigating regulatory requirements for veterinary therapeutics, and verifying long-term safety and efficacy.

Future directions should include proteomic and transcriptomic analyses of IVES-derived sEV cargo to pinpoint specific proteins, lipids, and nucleotides responsible for their therapeutic effects. Such studies would provide valuable insights into the molecular mechanisms underlying the anti-inflammatory and immunomodulatory properties of sEVs. Additionally, developing optimized formulations for long-term storage of sEVs at higher temperatures is essential to enhance their stability and shelf-life, particularly for field applications and commercial distribution. Standardizing protocols, integrating advanced bioreactor systems for large-scale production, and conducting comprehensive preclinical trials are critical steps for addressing these limitations and facilitating the successful clinical translation of sEV-based therapies.

Conclusion

This finding introduces a comprehensive refinement of the protocol for producing anti-inflammatory small extracellular vesicles (sEVs) from canine adipose-derived mesenchymal stem cells (cAD-MSCs). The innovative sequential stimulation method, termed IVES, involving low-oxygen gas mixture preconditioning using in vitro fertilization gas (IVFG) and direct current electrical stimulation (ES20), proves to be an effective tool for manipulating cellular processes. Our research successfully achieves efficient sEV production with biocompatibility, safety, and applicable purification. IVES induced a unique balance in gene expressions, inducting beneficial cellular modulation. Interestingly, *Hif1a* upregulations were attributed to ES20. Anti-inflammatory assessments revealed the potential of IVES in anti-inflammation at low immunogenicity, paving the way for therapeutic applications.

Methods

Isolation and expansion of cAD-MSCs

In adherence to ethical standards and with owner consent, adipose tissue was collected from a female German Shepherd dog (33.6 kg, 5 years old) at the Small Animal Teaching Hospital, Faculty of Veterinary Science, Chulalongkorn University, Thailand. Ethical guidelines set by the Institutional Animal Care and Use Committee (IACUC) of the Faculty of Veterinary Science were strictly followed, with approval granted under Animal Use Protocol 2231041. The collected adipose tissue was utilized for the isolation of canine adipose-derived mesenchymal stem cells (cAD-MSCs) as our previous study [34]. Tissues were minced, treated with Cell Recovery Solution (Corning, USA) for 2 h at 37 °C, and filtered through a 70 μm cell strainer (Corning, USA), followed by two washes with phosphate-buffered saline (PBS; Thermo Fisher Scientific, USA). The resulting cell pellets were resuspended and cultured in flasks (Corning, USA) containing the expansion media, Dulbecco's Modified Eagle Medium (Thermo Fisher Scientific, USA) supplemented with 10% fetal bovine serum (FBS; Thermo Fisher Scientific, USA), 1% GlutaMAX (Thermo Fisher Scientific, USA), and 1% Antibiotics-Antimycotic (Thermo Fisher Scientific, USA). Cultured cells were maintained at 37 °C with 5% CO_2, with media changed every 48 h. Subculturing using 0.25% trypsin (Thermo Fisher Scientific, USA) was performed when cells reached 80–90% confluence. Experimental studies utilized cells from passages 3–5.

Characterization of cAD-MSCs

Morphology of cAD-MSCs was observed under a phase-contrast microscope (Thermo Fisher Scientific, USA) at 40X and 200X magnifications. Additionally, MSC-related surface markers (CD29, CD44, and CD90) and a hematopoietic surface marker (CD45) were analyzed by flow cytometry. In particular, the cells were stained with PE-conjugated mouse anti-human CD29 monoclonal antibody (BioLegend, USA), Alexa Fluor 488-conjugated rat anti-dog CD44 antibody (BioRad, USA), PE-conjugated rat anti-dog CD90 monoclonal antibody (eBioscience, USA), and FITC-conjugated mouse anti-human CD45 antibody (BioLegend, USA). For the isotype controls, PE-conjugated mouse IgG1 kappa (BioLegend, USA), Alexa Fluor 488-conjugated rat IgG2a (BioRad, USA), PE-conjugated rat IgG2b kappa (eBioscience, USA), and PE-conjugated mouse IgG1 kappa (BioLegend, USA) were used,

respectively. The results were analyzed through a FACScalibur flow cytometer with CellQuest software (BD Bioscience, USA). Besides, mRNA expression profiling for stemness markers (*Oct4* and *Rex1*) and a proliferation marker (*Ki-67*) of non-stimulated cAD-MSCs was conducted using RT-qPCR.

For the Population Doubling Time (PDT) calculation of cAD-MSCs, representing the duration to double the cell population in passages 3–5, cells were cultured, trypsinized, and counted using a hemacytometer. PDT was computed using the formula: PDT = CTT/PDN. Here, CTT represents the time span from cell seeding to harvesting (days), and PDN is derived from PDN = log(N/N0) × 3.31, where N is the cell number at the end of the cultivation period, and N0 is the cell number at the initiation of the culture [95].

Multi-lineage differentiation potential of cAD-MSCs

The differentiation potentials of cAD-MSCs (passage 3) were determined using adipogenic, osteogenic, and chondrogenic induction protocols based on our prior studies [34, 35, 41, 96, 97]. In adipogenic differentiation, cAD-MSCs (3.0×10^4 cells/well) were seeded onto a 24-well culture plate (Corning, USA) and treated with adipogenic induction medium. The medium included 10% FBS (Thermo Fisher Scientific, USA), 0.5 µg/mL insulin (Sigma-Aldrich, USA), 1 µM dexamethasone (DEXA; Sigma-Aldrich, USA), 500 µM 3-isobutyl-1-methylxanthine (IBMX; Sigma-Aldrich, USA), and 100 µM indomethacin (Sigma-Aldrich, USA) for 28 days. Following this, intracellular lipid droplets were visualized using Oil Red O staining (Sigma-Aldrich, USA), and the expression of adipogenic mRNA markers (*Lep* and *Lpl*) was assessed by RT-qPCR.

For osteogenic differentiation, cAD-MSCs (2.5×10^4 cells/well) were seeded onto a 24-well culture plate (Corning, USA) and subjected to osteogenic induction. The induction medium contained DMEM (Thermo Fisher Scientific, USA) supplemented with 10% FBS (Thermo Fisher Scientific, USA), 50 µg/mL ascorbic acid (Sigma-Aldrich, USA), 0.25 µM dexamethasone (Sigma-Aldrich, USA), and 5,000 µM β-glycerophosphate (Sigma-Aldrich, USA) for 14 days [34, 35, 96]. Extracellular matrix mineralization was identified using Alizarin Red S dye (Sigma-Aldrich, USA), and osteogenic mRNA markers (*Ocn* and *Runx2*) were determined by RT-qPCR.

In chondrogenic differentiation, cAD-MSCs (5.0×10^4 cells/well) were seeded onto a 24-well culture plate (Corning, USA) and induced with chondrogenic medium. The medium comprised 15% FBS (Thermo Fisher Scientific, USA), 0.1 µM dexamethasone (Sigma-Aldrich, USA), 50 µg/mL ascorbic acid (Sigma-Aldrich, USA), 500 µg/mL L-proline (Sigma-Aldrich, USA), 0.02 µg/mL transforming growth factor (TGF)-β3 (Sigma-Aldrich, USA), and 1% insulin-transferrin-selenium (ITS; Thermo Fisher Scientific, USA) for 21 days [34, 35, 41, 96, 97]. Subsequently, glycosaminoglycan formation was detected by Alcian Blue staining (Sigma-Aldrich, USA), and the expression of chondrogenic mRNA markers (*Col2a1* and *Sox9*) was evaluated by RT-qPCR.

Establishment of electrical stimulation protocol

The protocol for electrical stimulation was established to produce small extracellular vesicles (sEVs) from cAD-MSCs under non-cytotoxic direct current (DC) power supply condition (Fig. 2A). The experimental setup, depicted in Fig. 2B, was adapted from previous studies [13, 23, 24]. Platinum wire auxiliary electrodes (Sigma-Aldrich, USA) were securely embedded in a 60-mm dish lid as an anode and a cathode with hot-melt adhesives. The electrodes were designated to contact with the media for 25 mm, while distance between the electrodes was set at 45 mm, resulting in an area of 1,125 mm^2 for electrical stimulation. The electrode lid was thoroughly sanitized by 70% alcohol wipes before UV irradiation for 30 min inside the BSC. Prior to stimulation, the electrodes underwent a washing process by soaking for 5 min in 5 mL of sterile deionized water filled in a 60-mm dish.

In this experiment, cAD-MSCs at passage 4 (1.2×10^5 cells/dish) were cultured on 60-mm dishes (Corning, USA), expanding in the media until reaching 70% confluence (6 days). After PBS wash, a 5 mL custom-mixed serum-free defined medium (VSCBIC-3) was filled into the dish. Inside the biosafety cabinet (BSC), a DC power supply (Extech Instruments, USA) was used to apply a constant electrical current to the cells via the electrodes submerged in the media. Stimulations occurred at room temperature (25 °C) for 30 min, employing different voltage supplies: ES0 (0 mV), ES20 (900 mV), and ES100 (4,500 mV).

The morphological appearances of electrical stimulated cAD-MSC were characterized using a phase-contrast microscope after stimulation with 100X magnification and before conditioned medium collection with 200X magnification. After a 24-h incubation period, the conditioned media were collected and stored at −80 °C until undergo purification within a week, in which the dedicated processes were stated in the section "Collection of conditioned media and purification of sEVs". To determine the potential of the established protocol for sEV production, particle size and concentration of the sEV samples were characterized by nanoparticle tracking analysis (NTA). To determine the cytotoxicity after treatments, the cells were trypsinized to count the viable cells by trypan blue exclusion assay.

Establishment of sequential stimulation of cAD-MSCs

In the sequential stimulation of cAD-MSCs for production of sEVs illustrated in Fig. 3A, cells at passage 5 (1.2×10^5 cells/dish) were cultured on 60-mm dishes (Corning, USA), expanding in the media until reaching 70% confluence (16 days). Following a PBS wash, cAD-MSCs underwent an 18-h pre-incubation with VSCBIC-3. The control condition (CTRL) continued incubation for 6 h, while in vitro fertilization gas preconditioning (IVFG) involved flowing humidified tri-gas (5% O_2, 6% CO_2, balance N_2; Thai Inter Gas and Chemical Supply, Thailand) through the dishes at 37 °C for 6 h, aiming to induce hypoxia conditions [15, 18]. This process occurred in the BioPipeline Live High Content Imaging System (Nikon, Japan) equipped with a CO_2 controller from the stage top incubator (OKOLAB, Italy). Notably, the CO_2 gas inlet was replaced by the tri-gas (0.05 VVM), as shown in Fig. 3B (left panel). For the electrical stimulation depicted in Fig. 3B (right panel), the DC power supply at 20 mV/mm (ES20) was employed at 900 mV for 30 min at room temperature (25 °C) according to the experimental setup mentioned above. Subsequently, cells were incubated under normal conditions for 5.5 h. In sequential stimulation (IVES), cAD-MSCs underwent ES20 immediately after IVFG. Lastly, the conditioned medium was collected for purification in further steps.

Characterization of stimulated cAD-MSCs

The morphological changes of treated cAD-MSC were characterized using the phase-contrast microscope at 200X magnification before conditioned medium collection. Then, cAD-MSCs were trypsinized for viable cell counting using trypan blue exclusion assay, where unstained cells were considered living. Before total cellular RNA collection with TRIzol™ reagent (Thermo Fisher Scientific, USA), cAD-MSCs were washed twice with PBS using centrifugation. The crude RNA samples were stored at −80 °C until further purification for subsequent RT-qPCR analysis. At this step, the mRNA expressions of biomarker for hypoxia condition (*Hif1a*), calcium homeostasis (*Hsp90b1*), exosome biogenesis (*Syntenin-1*), and endolysosomal trafficking (*Rab27b*) were considered.

Collection of conditioned media and purification of sEVs

The conditioned media obtained post-treatments were categorized as the Day1 sample (D1) to assess short-term effects on sEVs. Subsequently, fresh VSCBIC-3 was used for prolonged incubations, producing the Day2 and Day3 samples (D2D3) to observe long-term effects (Fig. 3A). These samples were stored at −80 °C until further steps in the purification process commenced within a week. For sEV purification, the frozen conditioned media were thawed in a water bath at 37 °C for 5 min, pooling Day2 and Day3 as the D2D3 sample, while Day1 remained unchanged. Preservation during purification was ensured by keeping samples at 4–6 °C or on ice. To eliminate cell debris and microvesicles, the sample passed through a 0.22-µm PDVF syringe filter (Merck, Germany) dropwise [54]. Subsequently, the filtrate underwent ultrafiltration with a 100-kDa centrifugal filter (Merck, Germany) per the manufacturer's protocol (5,000 RCF, 4 °C, 20 min) [55]. Buffer exchange (4X) was done by adding PBS into the filter device before sterilization via filtering with a 0.22-µm PDVF syringe filter (Merck, Germany). The sEVs were stored at −80 °C, and for thawing, the sample was placed in a water bath at 37 °C for 30 s prior to characterization or utilization.

Transmission electron microscopy (TEM)

To assess the morphology of sEVs isolated from cAD-MSCs, TEM was utilized. The sEV sample was diluted 10-fold in filtered PBS to prepare both 1.0X and 0.1X samples for negative staining with uranyl acetate [27]. For TEM preparation, 10 µL of the sEV sample was applied to a 400-mesh copper grid coated with a carbon-formvar film (Sigma-Aldrich, USA) and incubated for 5 min. Excess liquid was removed by blotting the grid with filter paper. Next, the grid was treated with a drop of 2% uranyl acetate (Merck, Germany) for negative staining, followed by blotting to remove the excess liquid. The grids were allowed to dry overnight. Imaging of the sEVs was performed using a Talos F200X microscope (Thermo Fisher Scientific, USA), operating at 200 kV, with images captured using Velox software.

Nanoscale flow cytometry

The exosomal surface marker of sEVs was analyzed using nanoscale flow cytometry with canine-specific CD9 labeling [98]. For staining, 45 µL of the sEV sample was incubated with 5 µL of Exobrite™ 410/450 conjugated anti-CD9 antibody (Biotium, USA) in the dark at room temperature for 30 min. An isotype control, IgG1 kappa antibody, was included for reference. Following incubation, 250 µL of 0.22-µm filtered PBS was added, and the sample was transferred to a FACS tube. The sample was analyzed using a DxFLEX flow cytometer (Beckman Coulter, USA) with a flow rate of 10 µL/min, reading 100,000 nanoparticle events based on violet side scatter (Violet SSC) at 405 nm. Initial gating for sEVs was performed using 300-nm polystyrene beads. CD9 positivity was determined by measuring fluorescence intensity at 450 nm in the Pacific Blue channel. The isotype control was used to facilitate gating of CD9-positive populations, with data analysis conducted using CytExpert 2.0.2.18 software (Beckman Coulter, USA).

Zeta-potential analysis

To estimate the electronegativity of sEVs as an indicator for particle stability [33], the sample underwent a tenfold dilution with PBS, resulting in a 3 mL sample volume for Zeta-potential determination. The analysis employed a disposable folded capillary cell and was performed at 25 °C. Using PBS as a dispersant, the Zeta-potential measurement was conducted on a Zetasizer Nano ZS (Malvern Instruments, UK).

Determination of protein concentration

Protein concentrations of sEV samples were measured using a Qubit™ Protein Assay kit (Invitrogen, USA) with some modifications. Briefly, the samples underwent denaturation in the low protein binding tube (Eppendorf, Germany) using a dry block heater at 75 °C for 10 min [99]. After vigorous mixing for 1 min, it was allowed to cool down at room temperature for 10 min before spinning down to collect the condensate. Subsequently, the Qubit™ working solution (180 µL) and the denatured sEV sample (20 µL) were mixed in the Qubit™ tube and incubated under dark condition at room temperature for 15 min. The fluorescent intensity was measured using a Qubit™ 3.0 Fluorometer (Invitrogen, USA) at 470 nm. The blank control of the analysis was PBS. As the protocol mentioned above, the calibration curve of bovine serum albumin (0, 10, 20 µg/mL, Biotium, USA) was prepared to calculate the protein concentration.

Nanoparticle tracking analysis (NTA)

To determine particle size and concentration of sEV sample, NTA was performed using the NanoSight NS300 (Malvern Panalytical, UK) equipped with a 405 nm laser module and sCMOS camera [100]. The concentrated sEV samples were diluted in 0.22-µm filtered PBS for ten folds, ranging from 10^7 to 10^9 particles/mL. Prior to analysis, the feeding tubing and the chamber of the laser module were sequentially rinsed with 70% ethanol and filtered PBS. The automated syringe pump (Harvard Bioscience, USA) allowed for recording a dynamic view of sEV representatives. The 60-second video of the laser scattering particles moving under Brownian motion was recorded at camera level 14.

The data was analyzed using NanoSight NTA 3.2 software with the detection threshold of 15. The particle size, modal hydrodynamic diameter, was estimated by tracking the particles in the video based on Stokes-Einstein equation [101]. The particle concentration was calculated from the particle number in the field of view from the video. In this research, the particle-to-cell ratio and the particle-to-protein ratio were considered as production yield of sEVs by cAD-MSCs and purity of sEV sample [56, 102, 103], respectively.

Anti-inflammatory activity of sEVs

The in vitro evaluation of anti-inflammatory activity for sEVs from cAD-MSCs followed established protocols [76, 77], focusing on LPS-stimulated RAW264.7 macrophages. This involved expanding cryopreserved RAW264.7 at passage 8 (ATCC, USA), seeding on a T-75 flask, and subsequently seeding at a density of 1.0×10^5 cells/well on a 96-well plate. After 24 h, the media were replaced with either 1,000 ng/mL LPS-containing media or LPS-free media. Various samples, including sEVs (1.5×10^8 particles/mL), positive control (1.25 µg/mL dexamethasone; Bukalo Trading, Thailand), and negative control (PBS; Sigma-Aldrich, USA), were added.

After an 18-h co-incubation, nitrite release in conditioned media was measured using nitrite assay. Briefly, 10 µL of Griess reagent (Biotium, USA), 65 µL of deionized water, and 75 µL of conditioned media were mixed and incubated at room temperature for 30 min in darkness. Absorbance at 570 nm was measured by using a microplate reader (Thermo Fisher Scientific, USA). After blank reduction (medium), the data from LPS-treated samples were subtracted from that of non-LPS-treated samples [77]. To calculate nitric oxide inhibition (NOI; %), the absorbance of LPS+ was subtracted by the individual value from LPS-, and the obtaining data of sample was divided by that of negative control and multiplied by 100. The immunogenicity of sEVs, were estimated by dividing the subtracted absorbance of non-treated sample with that of negative control to obtain the fold change in nitric oxide production [83]. The Eclipse Ti2 inverted microscope (Nikon, Japan) with 200X magnification was utilized for observing a microscopic appearance of the cells after co-incubation.

The viability of RAW264.7 was assessed using a resazurin assay. After discarding conditioned media, 120 µL of 150 µg/mL resazurin reagent (Sigma-Aldrich, USA) was added and incubated for 3 h. Subsequently, absorbances at 570 nm and 620 nm were measured by using a microplate reader (Thermo Fisher Scientific, USA). This assay incorporated a dual-wavelength spectrophotometric approach for correcting the resazurin reduction (RZR; %) using empirical absorbance ratios as described elsewhere [104]. To estimate relative cell viability (RCV; %), RZR of the sample was divided by that of the negative control and multiplied by 100 to obtain the percentage.

Quantitative reverse transcription polymerase chain reaction (RT-qPCR)

For mRNA analysis using RT-qPCR, total cellular RNA was extracted with TRIzol™ reagent (Thermo Fisher Scientific, USA) and the Direct-zol™ RNA Miniprep kit

(Zymo Research, USA) following the manufacturer's protocol. Subsequently, cDNA synthesis from RNA was conducted using the ImProm-II™ Reverse Transcription System (Promega, USA). Target genes were amplified and detected using PowerUp™ SYBR™ Green Master Mix (Applied Biosystems, USA) and the CF96™ real-time PCR detection system (BioRad, USA). Relative mRNA expression was determined by normalizing with glyceraldehyde-3-phosphate dehydrogenase (*Gapdh*) using the $2^{-\Delta Ct}$ approach. To calculate the fold change of the gene compared to the control group, the $2^{-\Delta\Delta Ct}$ method [105] was employed. Primers were designed using the NCBI primer designing tool based on mRNA sequences from the NCBI database (https://www.ncbi.nlm.nih.gov). The primer sequences and their accession numbers are provided in Supplementary Table S1.

Statistical analysis and data visualization

In this research, data are presented as mean ± standard error of the mean (SEM). Parametric datasets were analyzed using the t-test for two groups and one-way analysis of variance (ANOVA) for multiple groups. For non-parametric datasets, the Wilcoxon test compared two groups, and the Kruskal–Wallis test analyzed multiple groups. The Shapiro–Wilk test was applied for normality test of the datasets. Statistical significance at a 95% confidence interval was considered. R software (R Core Team, 2023) with the ggboxplot() function from the ggpubr package (version 0.6.0) was used for data visualization and statistical analysis. Linear regression was performed by executing the ggplot() function from the ggplot2 package (version 3.4.2). For Pearson's correlation coefficient matrix with linear regression, it was constructed by using the ggpairs() function from the GGally package (version 2.1.2).

Abbreviations

sEV	Small extracellular vesicle
MSC	Mesenchymal stem cell
cAD-MSC	Canine adipose-derived mesenchymal stem cell
IVFG	In vitro fertilization gas pre-conditioning
ES0	Electrical stimulation at 0 mV/mm
ES20	Electrical stimulation at 20 mV/mm
ES100	Electrical stimulation at 100 mV/mm
IVES	Sequential stimulation of IVFG and ES20
CTRL	Control condition
D1	sEV sample from Day1 collection
D2D3	Pooled sEV sample from Day2 and Day3 collections
SSC-A	Peak area of violet side scatter
CD9-PB450-A	Peak area of Pacific Blue-conjugated CD9 at 450 nm channel
NA	The data is not available
AU	Arbitrary unit
CD	Cluster of differentiation
VSCBIC-3	Custom-mixed serum-free defined medium
NTA	Nanoparticle tracking analysis
RT-qPCR	Quantitative reverse transcription polymerase chain reaction
DC	Direct current
LPS-	Non-LPS-induced condition
LPS+	LPS-induced condition
LPS	Lipopolysaccharide
NO	Nitric oxide
NOI	Nitric oxide inhibition
PBS	Phosphate buffered saline
RCV	Relative cell viability
DEXA	Dexamethasone
ISCT	International Society for Cellular Therapy
VVM	Volumetric flow rate
TEM	Transmission electron microscope
ESCRT	Endosomal sorting complexes required for transport
SMase	Ceramide-based sphingomyelinase
ATP	Adenosine triphosphate
TGF-β	Transforming growth factor beta
HIF-1α/2α	Hypoxia-inducible factor 1 alpha/2 alpha
OXPHOS	Oxidative phosphorylation
TRAF1	Tumor necrosis factor receptor-associated factor 1
MAPK	Mitogen-activated protein kinase
NF-κB	Nuclear factor kappa B
IACUC	Institutional Animal Care and Use Committee
FBS	Fetal bovine serum
PDT	Population doubling time
CTT	Time span from cell seeding to harvesting
PDN	Population doubling number
ITS	Insulin-transferrin-selenium
UV	Ultraviolet
kDa	kilo Dalton
RCF	Relative centrifugal force
PDVF	Polyvinylidene fluoride
sCMOS	Scientific complementary metal–oxide–semiconductor
RZR	Resazurin reduction
cDNA	Complementary DNA
SEM	Standard error of the mean
ANOVA	One-way analysis of variance

Supplementary Information

The online version contains supplementary material available at https://doi.org/10.1186/s12917-024-04465-2.

Supplementary Material 1: Table S1. Canine-specific primer sequences used in RT-qPCR for the determination of relative gene expression of cAD-MSCs. Figure S1. Pearson's correlation coefficient matrix of the relevant parameters obtained from the characterizations of cAD-MSC and sEVs after stimulation. The red boxes emphasize the significant correlation between parameters at 95% confidence intervals (p-value ≤ 0.05). Figure S2. Boxplot of the relative cell viability of RAW264.7 calculated from the resazurin assay in the determination of anti-inflammatory activity of cAD-MSC-derived sEVs. The macrophages were treated with lipopolysaccharides (LPS+) or without lipopolysaccharides (LPS-). The mean values of each group were annotated at the bottom, and global statistics were stated at the top. The bars indicate pairwise comparisons (****; p-value ≤ 0.0001).

Acknowledgements

The authors express gratitude to Mr. Noppadol Sa-Ard-Iam (BSc, MSc), Department of Periodontology, Faculty of Dentistry, Chulalongkorn University, for aid in flow cytometry analysis; and the Veterinary Stem Cell and Bioengineering Innovation Center (VSCBIC) (http://www.cuvscbic.com), Faculty of Veterinary Science, Chulalongkorn University, for research facility support. The author acknowledges the use of ChatGPT-3.5 and 4o, a large language model, in generating and refining content for this submission. The author takes complete responsibility for the content produced with the assistance of ChatGPT-3.5 and 4o and appreciates the potential of language models in enhancing scientific writing and knowledge dissemination.

Authors' contributions
S.O. contributed to the study design, conducted experiments, analyzed data, and wrote the manuscript. I.P. and Y.V.P. performed some experiments and contributed to manuscript revisions. P.S., W.R., P.S., T.P., B.N., N.S., D.N.N., T.O., H.E., and C.S. participated in the study design and provided critical revisions to the manuscript. All authors have read and approved the final manuscript.

Funding
This research is funded by Thailand Science Research and Innovation Fund Chulalongkorn University (FOOD66310024). In addition, this research project is supported by the Second Century Fund (C2F), Chulalongkorn University. The funders had no role in the conceptualization, design, data collection, analysis, decision to publish, or preparation of the manuscript.

Data availability
The datasets used and/or analyzed during the current study are available from the corresponding author on reasonable request.

Declarations

Ethics approval and consent to participate
The study adheres to ARRIVE guidelines and ethical standards set by the Institutional Animal Care and Use Committee (IACUC) of the Faculty of Veterinary Science. For tissue collection, the Animal Use Protocol 2231041 was approved by the Institutional Animal Care and Use Committee of the Faculty of Veterinary Science, Chulalongkorn University, Thailand, and explicit informed consent from owners was obtained before conducting adipose tissue biopsies.

Consent for publication
Not applicable.

Competing interests
The authors declare no competing interests.

Author details
[1]Second Century Fund (C2F), Chulalongkorn University for Post-doctoral Fellowship, Chulalongkorn University, Bangkok 10330, Thailand. [2]Center of Excellence for Veterinary Clinical Stem Cells and Bioengineering, Chulalongkorn University, Bangkok 10330, Thailand. [3]Veterinary Stem Cell and Bioengineering Innovation Center (VSCBIC), Veterinary Pharmacology, Stem Cell Research Laboratory, Faculty of Veterinary Science, Chulalongkorn University, Bangkok 10330, Thailand. [4]Department of Pharmacology, Faculty of Veterinary Science, Chulalongkorn University, Bangkok 10330, Thailand. [5]Center of Excellence in Systems Biology, Faculty of Medicine, Chulalongkorn University, Bangkok 10330, Thailand. [6]Department of Veterinary Biosciences and Veterinary Public Health, Faculty of Veterinary Medicine, Chiang Mai University, Chiang Mai 50100, Thailand. [7]Center of Excellence for Dental Stem Cell Biology, Faculty of Dentistry, Chulalongkorn University, Bangkok 10330, Thailand. [8]Department of Physiology, Faculty of Dentistry, Chulalongkorn University, Bangkok 10330, Thailand. [9]Department of Anatomy, Faculty of Dentistry, Chulalongkorn University, Bangkok 10330, Thailand. [10]Dental Stem Cell Biology Research Unit, Faculty of Dentistry, Chulalongkorn University, Bangkok 10330, Thailand. [11]Center of Excellence in Regenerative Dentistry (CERD), Faculty of Dentistry, Chulalongkorn University, Bangkok 10330, Thailand. [12]Center for Advanced Stem Cell and Regenerative Research, Division of Molecular and Regenerative Prosthodontics, Tohoku University Graduate School of Dentistry, Sendai 980-8575, Japan.

Received: 28 March 2024 Accepted: 30 December 2024
Published online: 21 January 2025

References

1. Kopper JJ, Iennarella-Servantez C, Jergens AE, Sahoo DK, Guillot E, Bourgois-Mochel A, et al. Harnessing the biology of canine intestinal organoids to heighten understanding of inflammatory bowel disease pathogenesis and accelerate drug discovery: A one health approach. Frontiers in Toxicology. 2021;3: 773953.
2. Wang J, Dai P, Zou T, Lv Y, Zhao W, Zhang X, et al. Transcriptome analysis of the transdifferentiation of canine BMSCs into insulin producing cells. BMC Genomics. 2021;22:1–5.
3. Kang SJ, Gu NY, Byeon JS, Hyun BH, Lee J, Yang DK. Immunomodulatory effects of canine mesenchymal stem cells in an experimental atopic dermatitis model. Front Vet Sci. 2023;10:1201382.
4. Tsouloufi TK, Theodorou K, Day MJ, Oikonomidis IL, Kasabalis D, Mylonakis ME, et al. Prevalence of antinuclear antibodies and rheumatoid factor titers in dogs with arthritis secondary to leishmaniosis (Leishmania infantum). J Vet Diagnostic Investig. 2022;34:699–702.
5. Kuwahara Y, Yoshizaki K, Nishida H, Kamishina H, Maeda S, Takano K, et al. Extracellular vesicles derived from canine mesenchymal stromal cells in serum free culture medium have anti-inflammatory effect on microglial cells. Front Vet Sci. 2021;8: 633426.
6. Park SM, An JH, Lee JH, Kim KB, Chae HK, Oh YI, et al. Extracellular vesicles derived from DFO-preconditioned canine AT-MSCs reprogram macrophages into M2 phase. PLoS ONE. 2021;16: e0254657.
7. An JH, Li Q, Bhang DH, Song WJ, Youn HY. TNF-α and INF-γ primed canine stem cell-derived extracellular vesicles alleviate experimental murine colitis. Sci Rep. 2020;10: e0254657.
8. Zhang Y, Le X, Zheng S, Zhang K, He J, Liu M, et al. MicroRNA-146a-5p-modified human umbilical cord mesenchymal stem cells enhance protection against diabetic nephropathy in rats through facilitating M2 macrophage polarization. Stem Cell Res Ther. 2022;13:171.
9. Hung CT, Racine-Avila J, Pellicore MJ, Aaron R. Biophysical modulation of mesenchymal stem cell differentiation in the context of skeletal repair. Int J Mol Sci. 2022;23:3919.
10. Cheng H, Huang Y, Chen W, Che J, Liu T, Na J, et al. Cyclic strain and electrical co-stimulation improve neural differentiation of marrow-derived mesenchymal stem cells. Front Cell Dev Biol. 2021;9: 624755.
11. Park KS, Bandeira E, Shelke GV, Lässer C, Lötvall J. Enhancement of therapeutic potential of mesenchymal stem cell-derived extracellular vesicles. Stem Cell Res Ther. 2019;10:1–5.
12. Kwon HJ, Lee GS, Chun H. Electrical stimulation drives chondrogenesis of mesenchymal stem cells in the absence of exogenous growth factors. Sci Rep. 2016;6:39302.
13. Mobini S, Leppik L, Parameswaran VT, Barker JH. In vitro effect of direct current electrical stimulation on rat mesenchymal stem cells. PeerJ. 2017;2017: e2821.
14. Tian J, Chen W, Xiong Y, Li Q, Kong S, Li M, et al. Small extracellular vesicles derived from hypoxic preconditioned dental pulp stem cells ameliorate inflammatory osteolysis by modulating macrophage polarization and osteoclastogenesis. Bioact Mater. 2023;22:326–42.
15. Ahmed NEMB, Murakami M, Kaneko S, Nakashima M. The effects of hypoxia on the stemness properties of human dental pulp stem cells (DPSCs). Sci Rep. 2016;6:35476.
16. Fawzy M, Emad M, AbdelRahman MY, Abdelghafar H, Abdel Hafez FF, Bedaiwy MA. Impact of 3.5% O2 culture on embryo development and clinical outcomes: a comparative study. Fertil Steril. 2017;108:635–41.
17. Bahir B, S. Choudhery M, Hussain I. Hypoxic preconditioning as a strategy to maintain the regenerative potential of mesenchymal stem cells. In: Regenerative Medicine. 2020.
18. Kling MJ, Chaturvedi NK, Kesherwani V, Coulter DW, McGuire TR, Sharp JG, et al. Exosomes secreted under hypoxia enhance stemness in Ewing's sarcoma through miR-210 delivery. Oncotarget. 2020;11:3633.
19. Rakesh R, PriyaDharshini LC, Sakthivel KM, Rasmi RR. Role and regulation of autophagy in cancer. Biochim Biophys Acta - Mol Basis Dis. 2022;1868: 166400.
20. Tandon N, Goh B, Marsano A, Chao PHG, Montouri-Sorrentino C, Gimble J, et al. Alignment and elongation of human adipose-derived stem cells in response to direct-current electrical stimulation. In: Proceedings of the 31st Annual International Conference of the IEEE Engineering in Medicine and Biology Society: Engineering the Future of Biomedicine, EMBC 2009. 2009.
21. Zhao Z, Watt C, Karystinou A, Roelofs AJ, McCaig CD, Gibson IR, et al. Directed migration of human bone marrow mesenchymal stem cells in a physiological direct current electric field. Eur Cells Mater. 2011;22:58.
22. Hardy JG, Villancio-Wolter MK, Sukhavasi RC, Mouser DJ, Aguilar D, Geissler SA, et al. Electrical stimulation of human mesenchymal stem cells on conductive nanofibers enhances their differentiation toward osteogenic outcomes. Macromol Rapid Commun. 2015;36:1884–90.
23. Eischen-Loges M, Oliveira KMC, Bhavsar MB, Barker JH, Leppik L. Pretreating mesenchymal stem cells with electrical stimulation causes sustained long-lasting pro-osteogenic effects. PeerJ. 2018;2018: e4959.

24. Hu M, Hong L, Liu C, Hong S, He S, Zhou M, et al. Electrical stimulation enhances neuronal cell activity mediated by Schwann cell derived exosomes. Sci Rep. 2019;9:4206.
25. Srirussamee K, Mobini S, Cassidy NJ, Cartmell SH. Direct electrical stimulation enhances osteogenesis by inducing Bmp2 and Spp1 expressions from macrophages and preosteoblasts. Biotechnol Bioeng. 2019;116:3421–32.
26. Zhao X, Ren H, Luo L. Gas bubbles in electrochemical gas evolution reactions. Langmuir. 2019;35:5392–408.
27. Rikkert LG, Nieuwland R, Terstappen LWMM, Coumans FAW. Quality of extracellular vesicle images by transmission electron microscopy is operator and protocol dependent. J Extracell Vesicles. 2019;8:1555419.
28. McVey MJ, Spring CM, Kuebler WM. Improved resolution in extracellular vesicle populations using 405 instead of 488 nm side scatter. J Extracell Vesicles. 2018;7:1454776.
29. Wang Y, Zhang L, Li Y, Chen L, Wang X, Guo W, et al. Exosomes/microvesicles from induced pluripotent stem cells deliver cardioprotective miRNAs and prevent cardiomyocyte apoptosis in the ischemic myocardium. Int J Cardiol. 2015;192:61–9.
30. Mostafa-Hedeab G, Hassan ME, Sabry D, Ali RI. Anti-diabetic therapeutic efficacy of mesenchymal stem cells-derived exosomes. Int J Pharmacol. 2020;16:437–46.
31. Sharun K, Muthu S, Mankuzhy PD, Pawde AM, Chandra V, Lorenzo JM, et al. Cell-free therapy for canine osteoarthritis: current evidence and prospects. Veterinary Quarterly. 2022;42:224–30.
32. Arévalo-Turrubiarte M, Baratta M, Ponti G, Chiaradia E, Martignani E. Extracellular vesicles from equine mesenchymal stem cells decrease inflammation markers in chondrocytes in vitro. Equine Vet J. 2022;54:1133–43.
33. Villatoro AJ, Alcoholado C, Martín-Astorga MDC, Rico G, Fernández V, Becerra J. Characterization of the secretory profile and exosomes of limbal stem cells in the canine species. PLoS ONE. 2020;15: e0244327.
34. Rodprasert W, Nantavisai S, Pathanachai K, Pavasant P, Osathanon T, Sawangmake C. Tailored generation of insulin producing cells from canine mesenchymal stem cells derived from bone marrow and adipose tissue. Sci Rep. 2021;11:12409.
35. Le Dang Q, Rodprasert W, Kuncorojakti S, Pavasant P, Osathanon T, Sawangmake C. In vitro generation of transplantable insulin-producing cells from canine adipose-derived mesenchymal stem cells. Sci Rep. 2022;12:9127.
36. Dominici M, Le Blanc K, Mueller I, Slaper-Cortenbach I, Marini FC, Krause DS, et al. Minimal criteria for defining multipotent mesenchymal stromal cells. The International Society for Cellular Therapy position statement. Cytotherapy. 2006;8:315–7.
37. Mitchell JB, McIntosh K, Zvonic S, Garrett S, Floyd ZE, Kloster A, et al. Immunophenotype of Human Adipose-Derived Cells: Temporal Changes in Stromal-Associated and Stem Cell-Associated Markers. Stem Cells. 2006;24:376–85.
38. Lindroos B, Boucher S, Chase L, Kuokkanen H, Huhtala H, Haataja R, et al. Serum-free, xeno-free culture media maintain the proliferation rate and multipotentiality of adipose stem cells in vitro. Cytotherapy. 2009;11:958–72.
39. Martinello T, Bronzini I, Maccatrozzo L, Mollo A, Sampaolesi M, Mascarello F, et al. Canine adipose-derived-mesenchymal stem cells do not lose stem features after a long-term cryopreservation. Res Vet Sci. 2011;91:18–24.
40. Kolf CM, Cho E, Tuan RS. Mesenchymal stromal cells. Biology of adult mesenchymal stem cells: Regulation of niche, self-renewal and differentiation. Arthritis Research and Therapy. 2007;9:204.
41. Nantavisai S, Rodprasert W, Pathanachai K, Wikran P, Kitcharoenthaworn P, Smithiwong S, et al. Simvastatin enhances proliferation and pluripotent gene expression by canine bone marrow-derived mesenchymal stem cells (cBM-MSCs) in vitro. Heliyon. 2019;5:e02663.
42. Sobecki M, Mrouj K, Colinge J, Gerbe F, Jay P, Krasinska L, et al. Cell-cycle regulation accounts for variability in Ki-67 expression levels. Cancer Res. 2017;77:2722–34.
43. Russell KA, Chow NHC, Dukoff D, Gibson TWG, La Marre J, Betts DH, et al. Characterization and immunomodulatory effects of canine adipose tissue- and bone marrow-derived mesenchymal stromal cells. PLoS ONE. 2016;11: e0167442.
44. Grzesiak J, Marycz K, Czogala J, Wrzeszcz K, Nicpon J. Comparison of behavior, morphology and morphometry of equine and canine adipose derived mesenchymal stem cells in culture. Int J Morphol. 2011;29:1012–7.
45. Nantavisai S, Pisitkun T, Osathanon T, Pavasant P, Kalpravidh C, Dhitavat S, et al. Systems biology analysis of osteogenic differentiation behavior by canine mesenchymal stem cells derived from bone marrow and dental pulp. Sci Rep. 2020;10:20703.
46. Sawangmake C, Nantavisai S, Osathanon T, Pavasant P. Osteogenic differentiation potential of canine bone marrow-derived mesenchymal stem cells under different β-glycerophosphate concentrations in vitro. Thai J Vet Med. 2016;46:617–25.
47. Mohamed-Ahmed S, Fristad I, Lie SA, Suliman S, Mustafa K, Vindenes H, et al. Adipose-derived and bone marrow mesenchymal stem cells: A donor-matched comparison. Stem Cell Res Ther. 2018;9:1–5.
48. Teshima T, Matsuoka A, Shiba M, Dairaku K, Matsumoto H, Suzuki R, et al. Comparison of properties of stem cells isolated from adipose tissue and lipomas in dogs. Stem Cells Int. 2019;2019:1609876.
49. Sasaki A, Mizuno M, Ozeki N, Katano H, Otabe K, Tsuji K, et al. Canine mesenchymal stem cells from synovium have a higher chondrogenic potential than those from infrapatellar fat pad, adipose tissue, and bone marrow. PLoS ONE. 2018;13: e0202922.
50. Arteaga-Blanco LA, Mojoli A, Monteiro RQ, Sandim V, Menna-Barreto RFS, Pereira-Dutra FS, et al. Characterization and internalization of small extracellular vesicles released by human primary macrophages derived from circulating monocytes. PLoS ONE. 2020;15: e0237795.
51. Geninatti T, Bruno G, Barile B, Hood RL, Farina M, Schmulen J, et al. Impedance characterization, degradation, and in vitro biocompatibility for platinum electrodes on BioMEMS. Biomed Microdevices. 2015;17:1–1.
52. Kamat GA, Zamora Zeledón JA, Gunasooriya GTKK, Dull SM, Perryman JT, Nørskov JK, et al. Acid anion electrolyte effects on platinum for oxygen and hydrogen electrocatalysis. Commun Chem. 2022;5:20.
53. Obata K, Van De Krol R, Schwarze M, Schomäcker R, Abdi FF. In situ observation of pH change during water splitting in neutral pH conditions: Impact of natural convection driven by buoyancy effects. Energy Environ Sci. 2020;13:5104–16.
54. Wang F, Cerione RA, Antonyak MA. Isolation and characterization of extracellular vesicles produced by cell lines. STAR Protoc. 2021;2: 100295.
55. Guerreiro EM, Vestad B, Steffensen LA, Aass HCD, Saeed M, Øvstebø R, et al. Efficient extracellular vesicle isolation by combining cell media modifications, ultrafiltration, and size-exclusion chromatography. PLoS ONE. 2018;13: e0204276.
56. de Almeida FM, Bernardes N, Oliveira FD, Costa AC, Fernandes-Platzgummer A, Farinha JP, et al. Scalable production of human mesenchymal stromal cell-derived extracellular vesicles under serum-/xeno-free conditions in a microcarrier-based bioreactor culture system. Front Cell Dev Biol. 2020;8: 553444.
57. Tognoli ML, Dancourt J, Bonsergent E, Palmulli R, de Jong OG, Van Niel G, et al. Lack of involvement of CD63 and CD9 tetraspanins in the extracellular vesicle content delivery process. Commun Biol. 2023;6:532.
58. Munir J, Yoon JK, Ryu S. Therapeutic miRNA-enriched extracellular vesicles: Current approaches and future prospects. Cells. 2020;9:2271.
59. Chen Y, Zhao Y, Yin Y, Jia X, Mao L. Mechanism of cargo sorting into small extracellular vesicles. Bioengineered. 2021;12:8186–201.
60. Sunil Kumar BV, Bhardwaj R, Mahajan K, Kashyap N, Kumar A, Verma R. The overexpression of Hsp90B1 is associated with tumorigenesis of canine mammary glands. Mol Cell Biochem. 2018;440:23–31.
61. Bando Y, Katayama T, Aleshin AN, Manabe T, Tohyama M. GRP94 reduces cell death in SH-SY5Y cells perturbated calcium homeostasis. Apoptosis. 2004;9:501–8.
62. Thomas R, Kim MH. HIF-1α: A key survival factor for serum-deprived prostate cancer cells. Prostate. 2008;68:1405–15.
63. Wang JA, Chen TL, Jiang J, Shi H, Gui C, Luo RH, et al. Hypoxic preconditioning attenuates hypoxia/reoxygenation-induced apoptosis in mesenchymal stem cells. Acta Pharmacol Sin. 2008;29:74–82.
64. Mathieu M, Martin-Jaular L, Lavieu G, Théry C. Specificities of secretion and uptake of exosomes and other extracellular vesicles for cell-to-cell communication. Nat Cell Biol. 2019;21:9–17.
65. Aheget H, Tristán-Manzano M, Mazini L, Cortijo-Gutierrez M, Galindo-Moreno P, Herrera C, et al. Exosome: A new player in translational nanomedicine. J Clin Med. 2020;9:2380.

66. Ortega FG, Roefs MT, de Miguel PD, Kooijmans SA, de Jong OG, Sluijter JP, et al. Interfering with endolysosomal trafficking enhances release of bioactive exosomes. Nanomedicine Nanotechnology, Biol Med. 2019;20: 102014.
67. Hao Z, Xu Z, Wang X, Wang Y, Li H, Chen T, et al. Biophysical stimuli as the fourth pillar of bone tissue engineering. Frontiers in Cell and Developmental Biology. 2021;9: 790050.
68. Wang K, Huang J, Chen H, Wang Y, Song S. Recent advances in electrochemical 2e oxygen reduction reaction for on-site hydrogen peroxide production and beyond. Chem Commun. 2020;56:12109–21.
69. Nouri F, Nematollahi-Mahani SN, Sharifi AM. Preconditioning of mesenchymal stem cells with non-toxic concentration of hydrogen peroxide against oxidative stress induced cell death: The role of hypoxia-inducible factor-1. Adv Pharm Bull. 2019;9:76.
70. White ESZ, Pennant NM, Carter JR, Hawsawi O, Odero-Marah V, Hinton CV. Serum deprivation initiates adaptation and survival to oxidative stress in prostate cancer cells. Sci Rep. 2020;10:12505.
71. Hanna C, Hubchak SC, Liang X, Rozen-Zvi B, Schumacker PT, Hayashida T, et al. Hypoxia-inducible factor-2α and TGF-β signaling interact to promote normoxic glomerular fibrogenesis. Am J Physiol - Ren Physiol. 2013;305:F1323–31.
72. Midekessa G, Godakumara K, Ord J, Viil J, Lättekivi F, Dissanayake K, et al. Zeta potential of extracellular vesicles: Toward understanding the attributes that determine colloidal stability. ACS Omega. 2020;5:16701–10.
73. Zheng X, Ai H, Qian K, Li G, Zhang S, Zou Y, et al. Small extracellular vesicles purification and scale-up. Front Immunol. 2024;15:1344681.
74. Amondarain M, Gallego I, Puras G, Saenz-del-Burgo L, Luzzani C, Pedraz JL. The role of microfluidics and 3D-bioprinting in the future of exosome therapy. Trends Biotechnol. 2023;41:1343–59.
75. Fan X, Fang S-B, Fu Q-L. Extracellular Vesicle-Based Clinical Trials. In: Wang Q, Zheng L, editors. Extracellular Vesicles: From Bench to Bedside. Singapore: Springer Nature Singapore; 2024. p. 541–53.
76. Malvicini R, Santa-Cruz D, De Lazzari G, Tolomeo AM, Sanmartin C, Muraca M, et al. Macrophage bioassay standardization to assess the anti-inflammatory activity of mesenchymal stromal cell-derived small extracellular vesicles. Cytotherapy. 2022;24:999–1012.
77. Oontawee S, Phonprapai C, Itharat A, Asasutjarit R, Davies NM. Mucus-penetrating nanovesicles encapsulating a novel anti-inflammatory recipe as a transmucosal remedy: Herbal extract preparation, synergistic combination, and niosomal encapsulation. J Herb Med. 2023;40: 100670.
78. Vishwakarma A, Wany A, Pandey S, Bulle M, Kumari A, Kishorekumar R, et al. Current approaches to measure nitric oxide in plants. J Exp Bot. 2019;70:4333–43.
79. Liu Y, Xu R, Gu H, Zhang E, Qu J, Cao W, et al. Metabolic reprogramming in macrophage responses. Biomarker Research. 2021;9:1–7.
80. Liang W, Han B, Hai Y, Sun D, Yin P. Mechanism of Action of Mesenchymal Stem Cell-Derived Exosomes in the Intervertebral Disc Degeneration Treatment and Bone Repair and Regeneration. Frontiers in Cell and Developmental Biology. 2022;9: 833840.
81. Jin QH, Kim HK, Na JY, Jin C, Seon JK. Anti-inflammatory effects of mesenchymal stem cell-conditioned media inhibited macrophages activation in vitro. Sci Rep. 2022;12:4754.
82. Dong B, Wang C, Zhang J, Zhang J, Gu Y, Guo X, et al. Exosomes from human umbilical cord mesenchymal stem cells attenuate the inflammation of severe steroid-resistant asthma by reshaping macrophage polarization. Stem Cell Res Ther. 2021;12:1–7.
83. Kverka M, Hartley JM, Chu TW, Yang J, Heidchen R, Kopeček J. Immunogenicity of coiled-coil based drug-free macromolecular therapeutics. Biomaterials. 2014;35:5886–96.
84. Lanci A, Iacono E, Merlo B. Therapeutic application of extracellular vesicles derived from mesenchymal stem cells in domestic animals. Animals. 2024;14:2147.
85. Heidarpour M, Krockenberger M, Bennett P. Review of exosomes and their potential for veterinary medicine. Res Vet Sci. 2024;168: 105141.
86. Yin Z, Qin C, Pan S, Shi C, Wu G, Feng Y, et al. Injectable hyperbranched PEG crosslinked hyaluronan hydrogel microparticles containing mir-99a-3p modified subcutaneous ADSCs-derived exosomes was beneficial for long-term treatment of osteoarthritis. Mater Today Bio. 2023;23: 100813.
87. An JH, Li Q, Ryu MO, Nam AR, Bhang DH, Jung YC, et al. TSG-6 in extracellular vesicles from canine mesenchymal stem/stromal is a major factor in relieving DSS-induced colitis. PLoS ONE. 2020;15: e0220756.
88. Liang X, Li C, Song J, Liu A, Wang C, Wang W, et al. HucMSC-Exo promote mucosal healing in experimental colitis by accelerating intestinal stem cells and epithelium regeneration via Wnt signaling pathway. Int J Nanomedicine. 2023;18:2799–818.
89. Shin KO, Ha DH, Kim JO, Crumrine DA, Meyer JM, Wakefield JS, et al. Exosomes from human adipose tissue-derived mesenchymal stem cells promote epidermal barrier repair by inducing de novo synthesis of ceramides in atopic dermatitis. Cells. 2020;9:680.
90. Kim SW, Lim KM, Cho SG, Ryu B, Kim CY, Park SY, et al. Efficacy of allogeneic and xenogeneic exosomes for the treatment of canine Atopic dermatitis: A pilot study. Animals. 2024;14:282.
91. Lee JH, Won YJ, Kim H, Choi M, Lee E, Ryoou B, et al. Adipose tissue-derived mesenchymal stem cell-derived exosomes promote wound healing and tissue regeneration. Int J Mol Sci. 2023;24:10434.
92. Zhou Y, Zhang XL, Lu ST, Zhang NY, Zhang HJ, Zhang J, et al. Human adipose-derived mesenchymal stem cells-derived exosomes encapsulated in pluronic F127 hydrogel promote wound healing and regeneration. Stem Cell Res Ther. 2022;13:407.
93. Tzng E, Bayardo N, Yang PC. Current challenges surrounding exosome treatments. Extracell Vesicle. 2023;2: 100023.
94. Wang J, Chen D, Ho EA. Challenges in the development and establishment of exosome-based drug delivery systems. J Control Release. 2021;329:894–906.
95. Tawonsawatruk T, Kanchanathepsak T, Duangchan T, Aswamenakul K, Supokawej A. Feasibility of bone marrow mesenchymal stem cells harvesting from forearm bone. Heliyon. 2021;7:e07639.
96. Sawangmake C, Nowwarote N, Pavasant P, Chansiripornchai P, Osathanon T. A feasibility study of an in vitro differentiation potential toward insulin-producing cells by dental tissue-derived mesenchymal stem cells. Biochem Biophys Res Commun. 2014;452:581–7.
97. Sawangmake C, Pavasant P, Chansiripornchai P, Osathanon T. High glucose condition suppresses neurosphere formation by human periodontal ligament-derived mesenchymal stem cells. J Cell Biochem. 2014;115:928–39.
98. Padda RS, Deng FK, Brett SI, Biggs CN, Durfee PN, Brinker CJ, et al. Nanoscale flow cytometry to distinguish subpopulations of prostate extracellular vesicles in patient plasma. Prostate. 2019;79:592–603.
99. Silva AM, Lázaro-Ibáñez E, Gunnarsson A, Dhande A, Daaboul G, Peacock B, et al. Quantification of protein cargo loading into engineered extracellular vesicles at single-vesicle and single-molecule resolution. J Extracell Vesicles. 2021;10: e12130.
100. Mizenko RR, Brostoff T, Rojalin T, Koster HJ, Swindell HS, Leiserowitz GS, et al. Tetraspanins are unevenly distributed across single extracellular vesicles and bias sensitivity to multiplexed cancer biomarkers. J Nanobiotechnology. 2021;19:250.
101. Desgeorges A, Hollerweger J, Lassacher T, Rohde E, Helmbrecht C, Gimona M. Differential fluorescence nanoparticle tracking analysis for enumeration of the extracellular vesicle content in mixed particulate solutions. Methods. 2020;177:67–73.
102. Hanai H, Hart DA, Jacob G, Shimomura K, Ando W, Yoshioka Y, et al. Small extracellular vesicles derived from human adipose-derived mesenchymal stromal cells cultured in a new chemically-defined contaminate-free media exhibit enhanced biological and therapeutic effects on human chondrocytes in vitro and in a mouse osteoarthritis model. J Extracell Vesicles. 2023;12:12337.
103. Li WJ, Chen H, Tong ML, Niu JJ, Zhu XZ, Lin LR. Comparison of the yield and purity of plasma exosomes extracted by ultracentrifugation, precipitation, and membrane-based approaches. Open Chem. 2022;20:182–91.
104. Goegan P, Johnson G, Vincent R. Effects of serum protein and colloid on the alamarBlue assay in cell cultures. Toxicol Vitr. 1995;9:257–66.
105. Schmittgen TD, Livak KJ. Analyzing real-time PCR data by the comparative CT method. Nat Protoc. 2008;3:1101–8.

Publisher's Note